Resistance to platinum chemotherapy in lung adenocarcinoma is driven by a non-genetic, cell-cycle dependent mechanism

Alvaro Gonzalez-Rajal[1#], Rachael McCloy[2], Max Nobis[2,4], Kamila A Marzec[1], Venessa Chin[2,3,4], Jordan F. Hastings[2], Kaitao Lai[1,5], Marina Kennerson[1,5] Vijesh Vaghjiani[6], William E Hughes[2], Paul Timpson[2,4], Jason Cain[6,7], D. Neil Watkins[8,9], David R. Croucher[2,4#] and Andrew Burgess[1,5#]

[1] *ANZAC Research Institute, Concord, NSW 2139, Australia*
[2] *The Kinghorn Cancer Centre, Garvan Institute of Medical Research, Sydney, NSW 2010, Australia.*
[3] *St Vincent's Hospital Sydney, Darlinghurst, NSW 2010, Australia*
[4] *St Vincent's Hospital Clinical School, University of New South Wales, Sydney, NSW 2052, Australia.*
[5] *The University of Sydney Concord Clinical School, Faculty of Medicine and Health, Sydney, NSW 2139, Australia*
[6] *Hudson Institute of Medical Research, Clayton, Victoria 3168, Australia.*
[7] *Department of Molecular and Translational Medicine, School of Medicine, Nursing and Health Sciences, Monash University, Clayton, Victoria 3800, Australia*
[8] *Research Institute in Oncology and Hematology, CancerCare Manitoba, Winnipeg, MB, Canada, R3E-0V9*
[9] *Department of Internal Medicine, Rady Faculty of Health Science, University of Manitoba, Winnipeg, Canada, R3E 0W2*

Running Title: Cell cycle dependent platinum resistance.

Keywords: 53BP1, PARP1, BRCA1, HR, ATR, PCNA, mitosis, DSB, NHEJ

Corresponding Authors:

Dr Alvaro Gonzalez-Rajal
Email: alvaro.gonzalezrajal@sydney.edu.au

A/Prof David Croucher
Email: d.croucher@garvan.org.au

A/Prof Andrew Burgess
Email: andrew.burgess@sydney.edu.au

Abstract:

Innate resistance to platinum-based chemotherapies has significantly reduced their impact in lung adenocarcinoma. We previously used a pulse-based *in vitro* assay to unveil targetable signalling pathways associated with this resistant phenotype (Hastings et al., 2020). Here we advanced this model system and identify a non-genetic mechanism of resistance that drives recovery and regrowth in a subset of cells. Using RNAseq and a suite of biosensors to track single cell fates both *in vitro* and *in vivo,* we identified that early S phase cells have a greater capacity to repair damage over multiple generations. In contrast, cells in G1, late S or those treated with PARP inhibitors, were unable to sufficiently repair the damage and underwent prolonged S/G2 phase arrest and senescence. These data indicate that there is a fundamental non-genetic mechanism of resistance in lung adenocarcinoma that is dependent on the cell cycle stage at the time of cisplatin exposure.

Introduction:

Lung adenocarcinoma (LUAD) is the most common form of lung cancer and the leading cause of cancer-related death in Australia. Less than 15% of patients have a targetable driver mutation and therefore cannot benefit from targeted therapy (Herbst et al., 2018). Consequently, the overwhelming majority of LUAD patients receive platinum-based chemotherapy as standard of care. The anti-tumour abilities of platinum compounds were first identified over 50 years ago with the discovery of cisplatin (Kelland, 2007). Since then, cisplatin and its derivatives have become one of the most successful groups of chemotherapeutics ever developed. Platinum therapy is essentially curative in testicular cancer, with survival rates >90%, and is also a frontline treatment for small-cell lung cancer, ovarian, head and neck, bladder, and cervical cancers (Kelland, 2007; Gonzalez-Rajal et al., 2020). Unfortunately, response rates to platinum in LUAD are below 30%, due mainly to innate resistance (Herbst et al., 2018). Nearly 150 different mechanisms of platinum resistance have been identified to date (Stewart, 2007). The vast majority of these mechanisms have been derived from preclinical models that utilise continuous, high dose exposure models, well above what is physiologically achievable in patients. Unsurprisingly, the majority of these models have failed to translate into improved clinical outcomes. To overcome this, we recently demonstrated that analysis of an *in vitro* assay that accurately models the *in vivo* drug exposure kinetics for cisplatin, could provide therapeutically

relevant insights into the signalling dynamics associated with innate resistance (Hastings et al., 2020). Cisplatin is given to patients as a single bolus dose, reaching a peak plasma concentration of ~14 μM, which is then rapidly cleared by the kidneys within 2-4 h (Andersson et al., 1996; Urien and Lokiec, 2004). We therefore mimicked this *in vitro* by pulsing cells for 2 h with the maximum plasma concentration (Hastings et al., 2020).

Once inside cells, platinum compounds can bind to DNA, RNA, and proteins (Gonzalez-Rajal et al., 2020), however the binding to DNA, which forms platinum-DNA adducts, are thought to be the primary mechanism for their tumour-specific killing. Intra-strand DNA-platinum adducts are repaired by base-excision and nucleotide excision repair during G1 (Slyskova et al., 2018). Inter-strand crosslinks (ICL) are removed largely by the Fanconi anemia (FA) pathway (Smogorzewska, 2019), which generates single and double strand breaks that are resolved by either the high-fidelity homologous recombination (HR) pathway during S-phase (Karanam et al., 2012) or by the error-prone non-homologous end joining (NHEJ) pathway during G1 and G2 phase (Enoiu et al., 2012; Slyskova et al., 2018). Consequently, targeting DNA repair pathways has become a major focus for enhancing platinum chemotherapies. For example, cells with defective HR repair have been shown to be highly sensitivity to combination therapy with cisplatin and PARP inhibitors in a number of cancer types including ovarian and breast (Tutt et al., 2018). However, correlation between cisplatin sensitivity and impaired DNA repair has often failed to translate clinically in LUAD (Mamdani and Jalal, 2016). In contrast, we have recently identified TGF-β (Marini et al., 2018) and P70S6K (Hastings et al., 2020) as key mediators of innate platinum resistance in LUAD. We now build upon these previous results and identify in this research advance that a sub-population of cells that are capable of continued proliferation despite exposure to pulsed cisplatin. Using a combination of cell cycle, DNA damage and replication biosensors combined with real-time single-cell fate tracking, we identified that these proliferative cells were enriched in late G1/early S phase at the time of cisplatin exposure and were able to sufficiently repair their DNA over multiple generations and rounds of replication. These results increase our understanding of the complexities underlying non-genetic resistance and recovery mechanisms in LUAD, while also highlighting mechanistic issues with a number of current clinical trials focused on combination therapy with cisplatin.

Results

Cells remain equally sensitive upon re-exposure to pulsed cisplatin.

In our previous work (Hastings et al., 2020), we identified several targetable signalling pathways that were associated with resistance to cisplatin in lung adenocarcinoma cells. In this work, our goal was to analyse the innate mechanisms that enable cell survival after exposure to cisplatin. To assess this, we analysed how cells respond to a subsequent dose of cisplatin, following recovery from an initial exposure event. To do this, we pulsed cells with cisplatin (5 µg/ml) and followed their response by time-lapse imaging. Cells were allowed to recover for 21-42 days (depending on their base rate of proliferation), before being challenged again with cisplatin, which equates to the approximate time patients normally receive a second dose in the clinic (Figure 1A). We utilised 3 LUAD cell lines: A549 (wild-type p53), NCI-H1573 ($p53^{R248L}$ mutant) and NCI-1299 (p53 null), which were all engineered to stably express Histone H2B fused to mCherry, allowing real-time quantitation of cell number and nuclear size. The initial pulse of cisplatin blocked the proliferation of A549 and NCIH1573 cells, and significantly reduced NCI-H1299 cell numbers over a 3-day period. This was mirrored in colony formation assays, with both A549 and NCI-1573 showing strong suppression of colony outgrowth, while p53-null H1299 cells were impacted to a lesser degree (Supplementary Figure S1A). Interestingly, there was a less noticeable effect on cell confluence (Figure 1B). Subsequent visual and quantitative analysis of cells by immunofluorescence revealed a corresponding 2 to 6-fold increase in total cell and nuclear area across all three cell lines (Figure 1C,D), accounting for the reduced impact on confluence. Following 21 days of recovery (42 days for NCI-H1573 due to slower rate of proliferation), cells appeared to return to their pre-pulse size (Figure 1C,D), with a subsequent cisplatin pulse resulting in a near identical response to the initial pulse, both in terms of inhibition of cell number, reduced confluence and increased cell size (Figure 1B-D). Based on these results, and our previous observation that all cells contained significantly increased levels of cisplatin-DNA adducts (Hastings et al., 2020), we concluded that cells surviving the first exposure remained equally sensitive to cisplatin and were therefore unlikely to have acquired resistance or arisen from an intrinsically resistant sub-clonal population within each cell line.

To assess this, we analysed the variability of cell and nuclear size after the initial pulse of cisplatin at 3-7 days post exposure. Visual analysis identified several colonies of cells whose size was similar to that of untreated control cells (Figure 2A). We hypothesised that these cells were able to proliferate and outgrow the non-proliferative (arrested) cells over the 21-42 day period. In support, a significant increase in senescence associated Beta-galactosidase (β-gal) staining was observed in A549 and to a lesser extent H1573 and H1299 cell lines (Figure 2 -Supplement 1B). Similarly, increased levels of the cyclin dependent kinase inhibitors p16 and p21, and increased senescence associated β-gal, were associated with larger cells across all 3 cell lines (Figure 2 -Supplement 1C), further indicating that larger cells have a lower proliferative capacity and are likely senescent. To test whether the surviving population arose from a subset of proliferating cells, we utilised the LeGo RGB colour-guided clonal cell tracking system (Weber et al., 2011). Briefly, each cell line was co-transfected with 3 different lentiviral vectors containing either a red, green or blue fluorescent protein. Each cell randomly received a variable amount of each plasmid resulting in a unique colour code for each cell. Quantitative colour analysis of untreated control cells revealed that up to 64 unique colours could be detected in each cell line. After pulsed exposure to cisplatin, single colour colony outgrowths were clearly visible in all 3 cell lines at 3-7 days post exposure, which was maintained at 21 or 42-days (Figure 2C). Taken together these results indicate that only a few colonies were responsible for repopulating the culture after the initial pulse exposure.

To confirm these results *in vivo*, we injected A549 or NCI-H1299 cells subcutaneously into the flanks of nude mice and allowed establishment of tumours (150 mm^3) before administering a single treatment of carboplatin (60 mg/kg). Mice harvested at 3 days post treatment were analysed by IHC for cell size and PCNA positive staining, with both cell lines showing a significant increase in cell size (Figure 3A, B). Similar to the *in vitro* results, active proliferation (PCNA positivity) in A549 cells was strongly suppressed after carboplatin exposure, indicating that the majority of cells were not proliferating. In contrast, H1299 cells, which lack p53 and only show mild reductions in proliferation *in vitro* (Figure 1B), did not show any significant decrease in PCNA staining *in vivo* (Figure 3A,B), but did significantly increase in cell size, closely matching results observed *in vitro.* In summary, these *in vitro* and *in vivo* data indicate that the majority of LUAD cells, especially those with functional

p53, become large and non-proliferative after pulsed treatment with cisplatin. Interestingly, a sub-population of cells remain at normal size, maintain their proliferative capacity, drive repopulation of the cell culture, and yet remain equally sensitive to successive cisplatin treatment, indicating a non-genetic mechanism of resistance.

Differential RNAseq analysis of cisplatin treated sub-populations

To better understand the potential mechanism driving the difference between cells that become large and senescent compared to those that maintain proliferative capacity, we performed RNAseq analysis on each unique population. Briefly, A549 cells were pulsed with cisplatin, harvested at 72 h and sorted by cell size using forward and side scatter parameters (FSC, SSC), with pre- and post-sorted cells then processed for RNAseq analysis (Figure 4A, B). Two-way hierarchical clustering indicated that there were clear differences between proliferative cisplatin treated cells compared to untreated control and non-proliferative cisplatin treated cells (Figure 4C). To better understand these effects, we undertook more detailed bioinformatic analysis using Ingenuity Pathway Analysis (IPA). Strong upregulation of the CDK inhibitor p21, was present in both pre-sorted cisplatin treated and post-sorted non-proliferative cells, matching the early flow data (Figure 2 Supplement 1C, Supplement Table 1,2). This corresponded with upregulation of p53, CHK and G2/M cell cycle checkpoint signalling, and a reduction in DNA replication and increase in senescence (Figure 4D, E), correlating with the increased β-gal and reduced proliferation observed above (Figure 2 Supplement 1B and Figure 1B). Importantly, proliferative cisplatin treated cells were significantly different from untreated controls, confirming our previous observation that that they were not simply cells that had avoided cisplatin exposure (Hastings et al., 2020). Notably, these proliferative cells displayed a decrease in EIF2, mTOR and p70S6K signalling, with a corresponding increase in TREM1, GP6 and IL-17F signalling pathways (Figure 4F, Supplement Table 3,4). Four-way comparative analysis further highlighted key differences between each sub-population, with proliferative cells all showing strong upregulation of BRCA1, ATM and DNA replication signalling pathways, which were heavily suppressed in non-proliferative cells (Figure 4G). Similarly, Gene Set Enrichment Analysis (GSEA), identified strong enrichment for cell cycle, HR directed repair, ATR and the Fanconi pathway in proliferative compared to arrested cells (Figure 4 Supplement 1A,B). In summary, these data suggest that the proliferative cells are considerably different from untreated control and

non-proliferative cells. Specifically, proliferative cells do not undergo significant p53/p21 dependent cell cycle checkpoint arrest but do show prominent upregulation of DNA repair pathways involving HR/BRCA1 and ATM/ATR.

Cell cycle status at time of exposure correlates with cell fate outcomes

The above RNAseq data indicated that there were strong cell cycle dependent differences between proliferative and non-proliferative cisplatin treated cells. To better understand these differences, we re-utilised the FUCCI biosensor system to enable real-time cell cycle status of individual cells (Hastings et al., 2020). Briefly, asynchronous A549 cells stably expressing FUCCI, were pulsed with or without cisplatin and then followed by time-lapse microscopy for 72 h. Individual cells were manually tracked and scored for cell cycle status and cell fate as previously described (Caldon and Burgess, 2019; Hastings et al., 2020). The majority of control cells divided at least 2 times within the 72 h time period (Figure 5 Supplement 1A,B). In contrast, cisplatin treated cells showed a range of cell cycle perturbations (Figure 5 Supplement 1A,C), including a significant and prolonged S/G2 phase arrest (Figure 5 Supplement 1D), which correlated with a reduced number of total divisions. However, as predicted by the LeGo and RNAseq data, there was a sub-population of cells that were able to undergo multiple (2 or more) divisions within the 72 h period, despite treatment with cisplatin. Interestingly, this population was enriched for cells in late G1 and early S-phase at the time of cisplatin exposure (Figure 5 Supplement 1A-D). This suggests that there is a cell cycle dependent mechanism driving the ability of cells to continue to proliferate after cisplatin exposure. To assess this in greater detail, we synchronised cells in either G1 or early S phase using either Palbociclib or thymidine, respectively (Figure 5A,B). Cells were then pulsed with cisplatin at various points following release to target G1, early or late S phase and then monitored by time lapse microscopy. Treatment of cells in G1 (Palbo + Cis at 0h) resulted in the majority of cells undergoing a prolonged S/G2 phase and then exiting back into a G1 like state without undergoing mitosis (G2-exit; Figure 5C), a state we described previously (Hastings et al., 2020). Notably, only 7/50 cells completed a single division and no cells underwent multiple (2 or more) divisions during the 72 h time period (Figure 5A,D). In contrast, treatment during late G1 (Palbo + Cis at 6h) and early S phase (Thy + Cis at -2h) resulted in significantly more cells (13/50 and 16/50 respectively) completing 2 or more divisions (Figure 5A-D). Finally, nearly all cells treated in late S phase

(Thy + Cis at 4h), completed the first mitosis and then underwent prolonged S/G2 arrest and G2-exit, with only 4 out of 50 cells completing 2 divisions within the 72 h period (Figure 5B-D). To validate these results *in vivo*, we implanted A549-FUCCI cells under optical windows in mice (Figure 5E). Tumours were allowed to establish before mice were given a single dose of carboplatin. Individual mice were then repeatedly imaged over 7 days post treatment. Notably, prior to cisplatin treatment, approximately 80% of cells were in G1 phase (Figure 5F-G). Similar to *in vitro* results, we observed a notable increase in S/G2 phase cells at day 1, indicating that cells were arrested in S/G2. This increase reduced from day 3 onwards, with over 90% of cells in a G1 like state at 7-days post treatment (Figure 5F-G). Taken together, these results indicate that cells in late G1 early S phase are capable of undergoing multiple cell cycle divisions, while cells in G1 or late S/G2 undergo prolonged S/G2 arrest and G2-exit both *in vitro* and *in vivo*.

Disruption of DNA repair reduces ability of early S phase cells to proliferate

The above data indicates that cells in late G1/early S phase at the time of cisplatin exposure are transiently resistant to cisplatin. A major target of cisplatin is DNA replication, with intra and inter-strand cross-links disrupting DNA replication, leading to stalled replication forks and the formation of double-strand breaks (Gonzalez-Rajal et al., 2020). We therefore hypothesised that cells in late G1/early S phase were able to repair cisplatin induced DNA damage during the first cell cycle more efficiently than cells in G1 or late S phase, thereby allowing them to continue to proliferate. To test this, we engineered A549 cells to stably co-express a truncated form of 53BP1 fused to mApple (Apple-53BP1trunc), which has previously been shown to bind double strand break sites co-marked with γH2A.X but lacks any of the functional domains of 53BP1 (Yang et al., 2015). We combined this with a PCNA Chromobody (Burgess et al., 2012) where we replaced GFP with mNeonGreen, to mark sites of active DNA replication (Figure 6A, inset). Cells were synchronised in early S phase with thymidine (as per Figure 5B), and then tracked by 4D-live cell imaging. Individual cells were divided into either those in G1, early-S or mid/late-S based on the pattern of PCNA foci (cyan), and then tracked through time. In control cells, a small number (<20) of 53BP1 positive foci (red hot) were observed as cells underwent the first round of replication (Figure 6A,B). Daughter and grand-daughter cells then displayed several (<5) large foci during G1 (up to 5 μm^2), which were resolved as cells entered S-phase and began replicating

(Figure 6C, white arrow). Cells that were in G1 at the time of cisplatin exposure, entered S-phase and rapidly accumulated a large number (~100) of 53BP1 positive foci, these slowly reduced over the remainder of the time-lapse (Figure 6A-C), which corresponded with an increase in the average size of the foci (~1 μm^2). In contrast, cells that were in early S-phase that completed multiple (2 or more) divisions within the 72 h timeframe, showed a rapid rise in foci number (~100), which then decreased at the conclusion of S phase, correlating with an increase in foci size. A small number of larger foci were present in the following G1 cell, although the size of these foci was smaller than those observed in control daughter cells (~1 μm^2). Interestingly, in grand-daughter and great grand-daughter cells, the size of G1 foci increased (>2 μm^2), in-line with G1 foci observed in control cells (Figure 6A-C, Figure 6 Supplement 1A). Finally, cells in mid-late S phase, also showed a large number of 53BP1 foci, which increased in size as cells progressed through the first G2 phase. Interestingly, the average number of 53BP1 foci were higher and were removed later, just prior to mitotic entry compared to cells from early S-phase (Figure 6A-C, Figure 6 Supplement 1B). Furthermore, the quality of mitosis was often reduced in cells from mid-S phase, with cells often presenting with chromatin bridges, micronuclei and/or failed cytokinesis (Figure 6 Supplement 1C), correlating with the increase in death during or after mitosis we observed previously (Figure 5C). The subsequent daughter cells from those exposed in mid-S phase then showed a rapid rise in the number of foci (>100) as they began replication. In contrast, the number of 53BP1 foci in early S-phase cells only increased mildly during replication and was notably lower than the numbers observed in the first round of replication (Figure 6 Supplement 1A,B). Based on these results, we concluded that early-S phase cells were able to either partially repair double strand breaks during the first round of DNA replication, and/or mark damage for efficient repair in the subsequent daughter and grand-daughter cells. In contrast, cells in G1 had much greater levels of damage and remained arrested in the first G2 phase. Cells in mid/late S phase completed the first division while acquiring damage but were unable to sufficiently repair the damage before mitosis. Consequently, daughter cells had un-repaired damage increased rates of mitotic induced breaks as they attempted the second round of DNA replication, leading to a strong S/G2 phase checkpoint arrest, similar to cells initially exposed during G1.

Based on these results, we hypothesised that cells in early-S phase were better able to take advantage of the high-fidelity homologous recombination (HR) pathway as replication forks encountered cisplatin adducts compared to G1 or late S phase. To test this, we utilised the PARP inhibitor, olaparib, to trap PARP at SSB sites, leading to increased rates of replication fork stalling and reduced capacity to repair DSBs by HR (Murai and Pommier, 2018). We hypothesised that this would increase the rate of damage in all cells and reduce the ability of early-S phase cells to repair during the first cell cycle. To test this, A549 FUCCI cells were synchronised in G1 or early S phase with Palbociclib or thymidine, as previously described (Figure 5A,B). Cells were then treated with or without Olaparib (PARPi) for 1 h prior to pulsed cisplatin exposure and monitored by time lapse microscopy (Figure 7A). In cells treated with cisplatin, co-treatment with PARPi significantly reduced the total number of divisions (Figure 7B), indicating that cells were unable to continue proliferating. This correlated with a trend toward a longer G1 phase in daughter cells in Palbociclib synchronised cells, and a highly significant G1 delay in thymidine synchronised cells (Figure 7C). Interestingly, although co-treatment with PARPi decreased the number of proliferative (2 or more divisions) cells there was only a small increase in death observed (Figure 7D), indicating that PARPi alone is not sufficient to drive increased toxicity to cisplatin in A549 cells. Importantly, inhibition of PARP did increase the rate of 53BP1 foci formation compared to cisplatin alone in asynchronous cells (Figure 7E). Furthermore, this correlated with a significant increase in both the amount of γ-H2AX staining and the size of cells (Figure 7F), indicating that PARPi was preventing efficient repair during the first replication cycle resulting in an increased rate of DNA damage and more pronounced S/G2 cell cycle checkpoint arrest.

Discussion:

In this work, we have identified a novel, non-genetic mechanism of resistance to platinum chemotherapy, which facilitates continued proliferation in a subset of cells after pulsed exposure to cisplatin. These cells eventually outgrow the majority of arrested cells over the course of 3 weeks *in vitro*. However, upon re-exposure, they remained equally sensitive, indicating that the mechanism of resistance is not hard-wired, nor did cells acquire resistance after the first exposure. Identification of these cells was largely dependent on the use of long-term quantitative single cell fate tracking (Caldon and Burgess, 2019), combined

with the use of a pulsed exposure model that closely mimics the *in vivo* kinetics of cisplatin in patients (Hastings et al., 2020). Tracing of individual cells that maintained proliferative capacity after pulsed cisplatin exposure, revealed a strong bias towards cells that were in late G1/early S phase at the time of exposure. In contrast, cells that were in early G1 arrested in S/G2 during the first replication cycle and underwent a G2-exit/senescent-like state. Notably, intracellular pH is lowest during G1, and cisplatin DNA binding is markedly increased in acidic conditions (Stewart, 2007), hence G1 phase cells likely have higher levels of cisplatin-DNA adducts, potentially explaining why these cells are unable to sufficiently repair and continue proliferating. In contrast, cells in mid-late S, G2 or M phase, proceed through the first division, attempt a second round of replication where they encounter higher levels of DNA damage, resulting in subsequent S/G2 phase arrest (Figure 8). Finally, cells in early S phase showed marked levels of double strand breaks during the first round of replication, however, the level of damage in daughter cells was significantly lower and returned to control levels in grand-daughter cells, explaining why these cells remained proliferative. Notably, had a continuous exposure model been used, cells in late G1/early S phase would have sustained cisplatin damage during all subsequent cell cycle stages, likely preventing the outgrowth of these clones, highlighting the importance of using *in vitro* systems that better reflect the *in vivo* pharmacokinetics of the chemotherapy.

The vast majority of cells both *in vitro* and *in vivo* are in G1 (>70%) or S-G2-M (~20%) at any given time, and hence the primary phenotype observed was that cells underwent prominent arrest and G2-exit during the first replication cycle. Conversely, the percentage of cells in late-G1/early S-phase is ~5-10%, which closely matches the low number of clones that continued to proliferate and repopulate the culture. Importantly, the ability of cells to maintain proliferative capacity was likely a function of the quality of repair and division, which in turn is dependent on the genetic background of each cell. In this regard the major cell cycle checkpoint response genes, such as p53, ATR and BRCA1/2 play important roles in determining how well cells respond to cisplatin exposure (Gonzalez-Rajal et al., 2020). For example, G1 treated A549 cells, which contain wild type p53, were able to instigate a strong p53 checkpoint response resulting in downstream upregulation of p21. This correlated with cells attempting to replicate their DNA, and a subsequent increase in 53BP1 positive foci indicating wide-spread induction of double strand breaks. Sustained p21 expression has

previously been linked to prolonged S/G2 phase arrest resulting in a G2-exit and senescence-like state in S/G2 (Baus et al., 2003). This decision is dictated at the individual cell level by the amount of DNA-damage and progress of repair. If damage is too great, then ATR-mediated checkpoint signalling results in sustained p21 expression, blocking CDK activity and preventing FOXM1 dependent G2 transcription required for mitotic entry (Saldivar et al., 2018). Notably the level of p21 induction observed in individual cells has been proposed to play a major role in determining if cells arrest, repair or continue cycling (Barr et al., 2017). Three major patterns of p21 expression have been observed after exposure to various chemotherapy treatments (Hsu et al., 2019). Surprisingly, cells that induce intermediate levels of p21 were more likely to maintain proliferative capacity, while those with initially low or high levels were more likely to become senescent. These states likely match the three major phenotypes we observed here, with G1 cells likely containing initially low levels of p21 that then rise after cells attempt DNA replication and repair, with cells in S-G2/M and early S-phase corresponding to high and intermediate levels, respectively. In support, we observed that cells in early S-phase have an initial wave of 53BP1 foci as they progress through S-phase, however daughter and grand-daughter cells showed far reduced levels. In contrast, daughter cells from those in S/G2 phase at the time of exposure showed heightened levels of damage. One possible explanation for this is that cells in S/G2 have already replicated large parts of their DNA when exposed, and hence these adducts many not be efficiently detected or repaired until after mitosis and the daughter cells undergo DNA replication (Figure 8). In contrast, early-S phase cells would encounter cisplatin adducts during the first replication cycle, initiate repair, most likely using homologous recombination, which is highest when cells are actively replicating during mid-S phase (Karanam et al., 2012). In contrast, error-prone NHEJ, which is preferred during G1 and G2, is likely favoured by cells exposed during G1 and late S-phase (Karanam et al., 2012). In support, proliferative cells were enriched for HR associated BRCA1-mediated signalling pathways compared to arrested cells. Interestingly, the first G2 phase was significantly longer in cells treated within mid/late S phase, suggesting some level of G2-checkpoint response and possible repair. However, cells eventually entered and progressed through an undelayed mitosis although numerous chromatin bridges were observed between separating daughter cells, which correlated with increased rates of mitotic and post-mitotic death. Chromatin bridges are often indicative of decatenation failure and

increased replication stress (Sarlós et al., 2017), which can lead to increased rates of cell death during or post mitotic division (Hayashi and Karlseder, 2013; Burgess et al., 2014). Notably, ultra-fine chromatin bridges (UFBs) are commonly formed after DNA damage caused by chemotherapies such as cisplatin. These can be repaired by homologous recombination, but if the repair is not completed before mitosis, then HR-intermediates result in the formation of UFBs (Chan et al., 2017; Chan and West, 2018). Consequently, cells exposed during early S-phase may have more time and capacity to avoid HR-UFBs during mitosis compared to those treated later in S-phase. In support, we observed delayed decrease in the rate of 53BP1 foci in mid/late S phase treated cells. While cells in early S-phase showed reduced levels of DNA damage (53BP1 positive foci) during second and third rounds of replication. Importantly, blocking and trapping PARP at sites of repair reduced the ability of cells to continue to proliferate, likely by disrupting HR-mediated repair during the first S phase. Taken together, this indicates that daughters of early S-phase treated cells have much lower levels of replication stress due to more efficient HR-mediated repair of cisplatin adducts during the first round of replication. Furthermore, post-mitotic G1 phase 53BP1 nuclear bodies increased in size from daughter to grand-daughter cells, indicating increasing efficiency in identification and corralling of unrepaired DNA damage during each replication cycle. These G1 53BP1 nuclear bodies prevent daughter cells from encountering damaged DNA during replication (Watt et al., 2020), thereby avoiding deleterious fork stalling. For under-replicated DNA, this provides the cell with a second chance at repair (Spies et al., 2019), and is likely the case for early S-phase cisplatin treated cells. The partial repair in the first cell cycle also likely ensures reduced p21 levels in subsequent cycles, helping promote continued proliferation. Notably, we previously demonstrated that in p53 mutant and null cells, p21 upregulation is compromised (Hastings et al., 2020), thereby impacting the ability of cisplatin to induce senescence in these cell lines. Interestingly, as observed in our previous paper, while p21/p53 are essential for determining cell cycle checkpoint response, they do not necessarily correlate with subsequent induction of apoptosis/cell death in LUAD cell lines. However, inhibition or knockdown of P70S6K did increase toxicity during this first division cycle (before mitosis), likely by reducing the threshold required to trigger cell death (Hastings et al., 2020). This potentially explains why co-inhibition of PARP - while preventing DNA repair, increasing the rate of DNA damage and reducing the ability of early S-phase cells to proliferate - was not able to enhance cisplatin

toxicity in A549 cells, due to high levels of P70S6K, which raise the death threshold in this cell line. Similarly, this work also indicates the potential for complications when co-administering platinum chemotherapies with Palbociclib. Specifically, pre or co-administration of Palbociclib with platinum may inadvertently synchronise cells in late G1/early S phase, resulting in a higher proportion of cells repairing the damage during the first cell cycle and maintaining proliferative capacity. In support, current clinical trials in head and neck cancer where both agents were given at the same time have resulted in no improvement to cisplatin therapy and resulted in significant treatment related toxicity (Swiecicki et al., 2020). Conversely, administering Palbociclib after cisplatin (and other chemotherapies), improves response and notably represses HR-dependent DNA repair (Salvador-Barbero et al., 2020). In summary, this work increases the understanding of the mechanisms driving recovery from cisplatin treatment and identifies the need for novel combination therapies that not only enhance cell death, but also prevent non-genetic, cell cycle dependent resistance mechanisms.

Materials and Methods:

Antibodies, Plasmids, and Reagents

The γH2A.X (S139)(AB26350), P16 (AB201980) and PCNA (AB29) antibodies were from Abcam (MA, USA). P21 antibody (2947) was purchased from Cell Signal Technology (MA, USA). Alexa-647 Conjugated Phalloidin antibody was purchased from ThermoFisher Scientific (A22287). The plasmids for FUCCI live cell imaging, mVenus-hGeminin(1/110) and mCherry-hCdt1(30/120), were a kind gift from Dr Atsushi Miyawaki (Riken, Japan). The LeGO plasmids were obtained from Addgene (#27338, #27339, #27340) (Weber et al., 2008). Thymidine (S4803), Olaparib (S1060), Palbociclib (S1116) were from Selleck Chem (MA, USA). Deoxycytidine (sc-231247) was from Santa Cruz Biotechnology (TX, USA).

Cell lines

All lung adenocarcinoma cell (LUAD) lines have been previously described (Marini et al., 2018). The lines were cultured in Advanced RPMI (Gibco, 12633012) containing 1% FCS and 1% GlutaMAX (35050– 061, Gibco) under standard tissue culture conditions (5% CO_2, 20%

449 O_2). All cell lines were authenticated by short tandem repeat polymorphism, single-
450 nucleotide polymorphism, and fingerprint analyses, passaged for less than 6 months.
451 Stable cell lines expressing the FUCCI biosensor were generated previously (Hastings et al.,
452 2020). H2B-mCherry cells were generated by lentiviral transfection, followed by FACS
453 sorting of low-expressing clones. Finally, dual Chromobody and 53BP1 A549 cells, were
454 generated by lenti-viral transfection with the PCNA-chromobody, with low expressing clones
455 isolated by cell sorting. These were then subsequently transfected (lentiviral) with truncated
456 form of 53BP1 fused to mApple (Apple-53BP1trunc), with cells resorted based on both
457 mNeonGreen and mApple to isolate dual expressing clones.
458
459 ***Colony Formation Assay and Senescence-Associated Beta-Galactosidase assay***
460 For colony formation assays, cells were seeded on 6 well plates, pulsed with cisplatin (or
461 not) and one to two weeks later, colonies were stained with 0.5% crystal violet and counted
462 using ImageJ/Fiji software. For β-Gal assays, cells were seeded on 6 well plates, pulsed with
463 cisplatin (or not) and fix and stained at 3 days following manufacture's protocol (Cell
464 Signaling Technology, #9860).
465
466 ***LeGO clonal analysis***
467 A549, NCI-H1573 and NCI-H1299 cells were transfected with LeGO lentiviral particles
468 (Addgene plasmids #27338, #27339, #27340)(Weber et al., 2008) following the method
469 described in (Weber et al., 2012). Cells were treated with/without cisplatin and images were
470 taken at 3 days and at 21 days (A549 and NCI-H1299) or 42 days (NCI-H1573) after cisplatin
471 exposure. 100 images were taken per timepoint and per condition (3 replicates) and the
472 experiment was done twice. The total number of clones (unique colour cues) and the
473 number of cells within each clone was determine. Briefly, images are opened and converted
474 to 16bit.tif files. An image is duplicated and converted to RGB overlay. The duplicate has
475 background subtracted using a rolling ball at 250 considering colours separately and using a
476 sliding parabaloid. The image is smoothed using a mean filter radius 5. Using the "find
477 maxima" function a point withing individual cells is identified and then enlarged to a circle
478 radius 5 pixels. These ROI are then applied as a mask to the unprocessed, raw, image data
479 and the average red, green and blue values within these ROI collected and exported in .csv
480 format. RGB values from each of the .csv files for each of the 100 images are complied. Data

from cells where an R, G or B value is too high or too low are removed. 512 unique colours were identified and cells were classified and assigned to each of the 512 colours. More than 90% of all cells were assigned to one of the 64 most represented colours, therefore the following analysis was performed using these 64 groups

Animal Experiments

Animal experiments were conducted in accordance with the Garvan/St Vincent's Animal Ethics Committee (guidelines ARA 18_17, ARA_16_13) and in compliance with the Australian code of practice for care and use of animals for scientific purposes. Mice were kept in standard housing at a 12h day light cycle and fed ad libitum. Cage enrichment refinement was undertaken with mice implanted with mammary optical imaging windows, supplying the fully plastic IVC cages with papier-mâché domes, feeding supplied in trays on the cage floor and soft tissues as nesting material. For *in vivo* xenograft models A549 cells ($2x10^6$) were resuspended in 100 µL PBS:Matrigel (1:1) and injected subcutaneously into the flanks of of BALB/c-Fox1nuAusb mice (Australian BioResource). Tumour growth was assessed twice weekly by calliper measurement and mice were randomized to treatment arms when tumours reached 150 mm3 (using the formula: $width^2$ x length x 0.5). Carboplatin (60 mg/kg) was delivered by a single i.p injection. Tumours were harvest at 3-7 days post treatment and analysed by IHC for cell size and PCNA positive staining.

Implantation of Optical imaging windows

BALB/c-Foxn1nu/Ausb mice were injected with $1x10^6$ A549-Fucci subcutaneously near the inguinal mammary fat pad. Following the development of palpable tumours, mice were engrafted with titanium mammary imaging windows (Russell Symes & Company) as described previously (Kedrin et al., 2008; Gligorijevic et al., 2009; Ritsma et al., 2013; Nobis et al., 2017). Briefly, mice were treated with 5 mg/kg of the analgesic Carprofen (Rimadyl) in pH neutral drinking water 24h prior and up to a minimum of 72h post-surgery. Mice further received subcutaneous injections of buprenorphine (0.075mg/kg, Temgesic) immediately prior and 6h post-surgery. The titanium window was prepared 24h prior to surgery by gluing a 12mm glass coverslip (Electron Microscopy Science) using cyanoacrylate to the groove on the outer rim of the titanium window. Following anaesthetic induction at 4% isoflurane delivered via a vaporizer (VetFlo) supplemented with oxygen, mice were kept at a steady 1-

2% maintenance anaesthesia for the duration of the surgery on a heated pad. The incision site was disinfected using 0.5% chlorhexidine/ 70% ethanol. A straight incision was made into the skin above the developed subcutaneous tumour and following blunt dissection of the skin surrounding the incision a purse string suture (5-0 Mersilk, Ethicon) placed. The windows were then inserted and held in place by tightening the suture, disappearing along with the skin into the groove of the window and tied off. Mice were allowed to recover for a minimum of 72h post-surgery, actively foraging, feeding and grooming within minutes from being removed from the anaesthesia respirator. A minimum of 24h prior to imaging and treatment mice were weaned off the Carprofen analgesic in the drinking water.

In vivo imaging

Mice were imaged under 1-2% isofluorane on a heated stage (Digital Pixel, UK) prior to and 1 day, 2 days, 3 days and 7 days after ip injection of 60 mg/kg Carboplatinum (Sigma) or the saline vehicle. Multi-photon imaging was performed using a Leica DMI 6000 SP8 confocal microscope using a 25x 0.95 NA water immersion objective on an inverted stage. For A549-Fucci imaging the Ti:Sapphire femto-second laser (Coherent Chameleon Ultra II, Coherent) excitation source operating at 80MHz was tuned to 920 nm and the RLD-HyD detectors with 460/40, 525/50 and 585/40 bandpass emission filters used to detect the second harmonic generation (SHG) of the collagen I, mAzamiGreen and mKO2 respectively. Images were acquired at a line rate of 400 Hz, 512x512 pixel and a line average of 8.

Flow cytometry Analysis and Sorting

Samples for flow cytometry were fixed in -20°C ethanol overnight, and then stained with a primary antibody against p21 (Cell Signal Technology, 2947), p16 (Abcam, ab201980) or γH2A.X (S139)(Abcam, ab26350) and following an incubation with an Alexa Fluor 647 secondary antibody (Invitrogen). Flow cytometry was performed using a Beckman CytoFlex S. For senescence assays we used ImaGene Green™ C12FDG lacZ Gene Expression Kit (Molecular probes, I-2904). Three days after cisplatin exposure cells were incubated for 30 min with Bafilomycin A1 (Sigma, B1793) in RPMI medium without phenol red (Gibco) supplemented with 1% FBS before adding C_{12}FDG to the media at 20 µM final concentration. Cells were incubated for 60 minutes prior to 15 minutes fixation with PFA 4% and processed for FACS analysis. Flow cytometry was performed using a Beckman CytoFlex

S. For cell sorting and RNAseq analysis, A549 cells were treated with or without cisplatin (5 mg/mL) for 2 hr, and then allowed to recover for 3-days. Cells were harvested and sorted based in their size (FSC vs SSC) using a BD FACS Aria IIu. Sorted cells were frozen as pellet in dry ice and stored at -80^{o}C until RNA purification.

Immunofluorescence and live cell imaging

Cells were grown on Histogrip (Life Technologies) coated glass coverslips and fixed with 3.7% formaldehyde diluted in PHEM buffer (60 mM Pipes, 25 mM hepes, 1 mM EGTA, 2 mM MgCl2) with 0.5% Triton X-100 for 10 min. All cells were washed and then blocked (3% BSA, 0,1% Tween 20 in PBS) for 30 min. Cells were incubated with primary antibodies were incubated for 2 h at room temperature in blocking solution. DNA was stained with H33342 and imaged using a imaged using an EVOS FL2 Auto Imager (Thermofisher) or a Leica SP8-X confocal with white light laser using either a 20X (NA 0.75) or 63X (NA 1.40) objectives. In some cases, 0.3 µm Z-sections were taken and displayed as 2D slices or maximum projections using Fiji (Image J v2.1.0/1.53c) and compiled using Adobe Photoshop CC 2020 software. Deconvolution and 3D volume renderings performed using Huygens Professional Software (Scientific Volume Imaging, v20.04), while nuclear size analysis was performed using StarDist (Schmidt et al., 2018) plugins for Fiji/ImageJ. Live cell imaging and IncuCyte (Sartorius) proliferation assays were performed as previously described (Hastings et al., 2020). Briefly, for live cell imaging, cells were seeded at 35% confluence on 6 or 12 well plates and imaged using a Leica DMI6000 using a 20X NA 0.4 objective. Images were taken every 10-20 min for up to 72 h. Individual cells were followed and scored for nuclear envelope breakdown (NEBD) and first signs of anaphase as previously described (Caldon and Burgess, 2019). Mitotic length = NEBD to anaphase, while interphase length = anaphase to next daughter cell NEBD. Only the first daughter cell to divide was followed and annotated. For IncuCyte assays, cells were seeded on 12 or 24 well plates and filmed for up to 4 days at 4 h intervals. Confluence and nuclear masks were generated and used to determine cell proliferation as previously described (McCloy et al., 2014). For 53BP1 and PCNA chromobody experiments, cells were seeded on 8-Well Ibidi Polymer Coverslip µ-Slides (#80826), synchronised with thymidine or Palbociclib and pulsed with cisplatin for 2 h, before imaging on a Lecia SP8 confocal microscope fitted with a white light laser, hybrid detectors (HyD), a 63X HC PL APO CS2 (NA 1.40) objective and stage top incubator system

set at 37C and 5% CO_2. Multiple X/Y positions, and a 10 µm z-stack (1 µm z-section) taken every 30 min for 72 h, with 4D deconvolution and volume rendering performed with Huygens Professional (v20.04) software (Netherlands). 53BP1 and PCNA foci analysis was performed on 2D-maximim intensity projections using appropriate thresholds coupled with analyse particles module within ImageJ/Fiji. The pattern of PCNA foci was used to position cells in early, mid or late S phase, as previously described (Burgess et al., 2012; Charrasse et al., 2017).

Immunohistochemistry

Immunohistochemistry was performed on formalin fixed paraffin embedded sections using the Leica BOND RX (Leica, Wetzlar, Germany). Slides were first dewaxed and rehydrated, followed by heat induced antigen retrieval performed with Epitope Retrieval Solution 1 BOND (Leica, Wetzlar, Germany). PCNA Primary antibody was diluted 1:500 (Abcam, ab29) in Leica antibody diluent and incubated for 60 min on slides. Antibody staining was completed using the Bond Polymer Refine IHC protocol and reagents (Leica, Wetzlar, Germany). Slides were counterstained on the Leica Autostainer XL (Leica, Wetzlar, Germany). Leica CV5030 Glass Coverslipper (Leica, Wetzlar, Germany) and brightfield images were taken on the Aperio CS2 Slide Scanner (Leica, Wetzlar, Germany). Quantification of PCNA staining was performed on three fields of view for each tumour section.

RNA isolation, RNA sequencing (RNA-seq), SNV alignment and analysis

Cell pellets were obtained from the different conditions/populations. Cell pellets were frozen in dry ice prior to storage at -80°C. Total RNA was purified using miRNeasy Micro Kit (Qiagen, 217084) following the manufacture's protocol, including a DNase treatment. RNA concentration and quality were also measured by Qubit and Nanodrop. Samples were only used if they showed a 260/280 ratio >2.0 (Nanodrop). RNA integrity was determined on an Agilent 2100 Bioanalyser and samples were only used if they showed a RIN of >8. Three sets of RNA were collected per condition. Compliant samples were sent to the Australian Genome Research Facility (AGRF) for RNA sequencing with poly(A) selection. Briefly, 20 million 100 bp single end RNA-seq was conducted on an Illumina NovaSeq platform. The library was prepared using the TruSeq stranded RNA sample preparation protocol (Illumina).

609 The cleaned sequence reads were aligned against the *Homo sapiens* genome (Build version
610 hg38) and the RNA-seq aligner, "Spliced Transcripts Alignment to a Reference (STAR)"
611 aligner (v2.5.3a) (Dobin et al., 2013), was used to map reads to the genomic sequence.
612 Transcripts were assembled using the StringTie tool v1.3.3 (Pertea et al., 2015) with the
613 read alignment (hg38) and reference annotation-based assembly option (RABT). Raw data
614 were deposited in the NCBI Gene Expression Omnibus (GEO) data repository accession
615 number GSE161800.
616
617 The raw data from each cell line was aligned to the human genome reference build
618 GRCh38/hg38 using STAR aligner v2.5.3a by AGRF. Single Nucleotide Variations (SNVs) were
619 identified using SNV caller Freebayes (v1.3.1; https://github.com/ekg/freebayes) and
620 annotated using Bcftools (v1.9)(Danecek and McCarthy, 2017) with database NCBI dbSNP
621 (v146)(Sherry et al., 2001). Heatmaps, principal component analysis (PCA) and biological
622 coefficient variant plots were made using R language and software (The R Foundation) with
623 the DESeq2 package (Love et al., 2014). The log2 (fold change) scale was normalised and
624 transformed by considering library size or other normalisation factors. The transformation
625 method and the variance stabilising transformation (VST) (Anders and Huber, 2010) for over
626 dispersed counts have been applied in DESeq2. The VST is effective at stabilising variance,
627 because it considers the differences in size factors, such as the datasets with large variation
628 in sequencing depth (Love et al., 2014). Canonical Pathway analysis of known proliferation,
629 cell cycle, migration and cell death-related signalling pathways were conducted using the
630 Ingenuity Pathway Analysis software (QIAGEN), as previously described (Johnson et al.,
631 2020). Briefly, minimum significance cut offs of p-value>0.05 and Z scores of >2 and <-2
632 were applied for pathways analysis. For Gene Set Enrichment Analysis (GSEA) a ranked gene
633 list was prepared from Proliferative versus Arrest and analysed with GSEA 4.1.0 software
634 (https://www.gsea-msigdb.org/gsea/index.jsp) using a curated gene set of canonical
635 pathways (2868 gene sets) (https://www.gsea-msigdb.org/gsea/msigdb/collections.jsp#C2)
636 (Mootha et al., 2003; Subramanian et al., 2005). The enrichment map was generated using
637 Cytoscape 3.8.2 software (https://cytoscape.org/)(Shannon et al., 2003), using p-value
638 (<0.005) and FDR (q<0.1) cut offs. Volcano and dot plots were generated using GraphPad
639 PRISM (v9.0.0) and figures compiled using Adobe Illustrator (v25).
640

Acknowledgements

The authors would like to acknowledge Dr Atsushi Miyawaki (Riken, Japan) for provision of the mVenus-hGeminin(1/110) and mKO-hCdt1(30/120) constructs for FUCCI imaging. Dr Liz Caldon for her insightful and helpful comments. The Patricia Helen Guest Fellowship for their generous support. The authors acknowledge the ANZAC Microscopy and Flow Facility, the Sydney Informatics Hub and the use of the University of Sydney's high performance computing cluster, Artemis.

Additional Information

Funding:

Cancer Institute NSW	2013/FRL102	David R Croucher
Cancer Institute NSW	15/REG/1-17	David R Croucher
Cancer Institute NSW	10/FRL/3-02	Andrew Burgess
National Breast Cancer Foundation	IIRS-18-103	Andrew Burgess
Tour de Cure	RSP-230-2020	Andrew Burgess

The funders had no role in study design, data collection and interpretation, or the decision to submit the work for publication.

Author contributions

Alvaro Gonzalez Rajal, Conceptualization, Data curation, Formal analysis, Visualization, Methodology; Rachael A McCloy, Formal analysis, Investigation, Methodology; Max Nobis, Formal analysis, Visualization, Methodology; Kamila A Marzec, Data curation, Formal analysis, Visualization; Venessa Chin, Resources, Data curation, Supervision, Investigation, Methodology; Jordan F. Hastings, Formal analysis, Visualization; Kaitao Lai, Formal analysis, Visualization, Data curation; Marina Kennerson, Supervision, Methodology; Vijesh Vaghjiani, Data curation, Formal analysis; William E Hughes, Data curation, Formal analysis; Paul Timpson, Supervision, Methodology; Jason Cain, Data curation, Formal analysis, Supervision, Methodology; D Neil Watkins, Conceptualization, Supervision, Methodology, Data curation, Formal analysis, Visualization; David R Croucher, Conceptualization, Formal analysis, Supervision, Funding acquisition, Investigation, Project administration; Andrew

672 Burgess, Conceptualization, Formal analysis, Supervision, Validation, Investigation,
673 Visualization, Methodology, Project administration, Funding acquisition.
674
675 **Author ORCIDs**
676 Alvaro Gonzalez-Rajal: https://orcid.org/0000-0002-9230-0339
677 Rachael McCloy: https://orcid.org/0000-0001-7791-4044
678 Max Nobis: https://orcid.org/0000-0002-1861-1390
679 Venessa Chin: https://orcid.org/0000-0002-4630-4451
680 Kamila A. Marzec: https://orcid.org/0000-0002-3051-2205
681 Marina Kennerson https://orcid.org/0000-0003-3332-5074
682 Kaitao Lai https://orcid.org/0000-0002-9420-9352
683 D. Neil Watkins: https://orcid.org/0000-0001-8218-4920
684 David R Croucher https://orcid.org/0000-0003-4965-8674
685 Andrew Burgess https://orcid.org/0000-0003-4536-9226
686
687 **Animal experimentation:** All experiments were carried out in compliance with the
688 Australian code for the care and use of animals for scientific purposes and in compliance
689 with Garvan Institute of Medical Research/St. Vincent's Hospital Animal Ethics Committee
690 guidelines (ARA_18_17, ARA_16_13).
691
692 **Figure Legends:**
693 **Figure 1 – Rechallenging LUAD cells with cisplatin results in similar response profiles. (A)**
694 Schematic of rechallenging experiments. Briefly, cells stably expressing H2B-mCherry were
695 pulsed with 5µg/ml cisplatin for 2 h. Cell proliferation (nuclear number and cell size) were
696 then tracked for up to 4-days. Cells were then allowed to recover for 21 (A549 and NCI-
697 H1299) or 42 days (NCI-H1573), re-culturing once confluent, before being re-pulsed with
698 cisplatin. **(B)** Cell confluence and cell number were tracked over for up to 4-days using by
699 IncuCyte based time-lapse imaging. Shown are the mean +/- SD of 3 biological repeats. **(C)**
700 Immunofluorescence of cells at 72 h post cisplatin treatment. Nuclei = cyan, β-tubulin = red,
701 scale bar = 10µm. **(D)** Quantification of cell size and nuclear size from A, with a minimum of
702 200 cells analysed per condition. Shown are the mean+/- SD. Statistical significance was
703 determined by one-way ANOVA (****p<0.0001, n.s = not significant).

Figure 2 – Variable cell size and clonal outgrowth in post-cisplatin treated cells. (A) Representative images from cells treated as per Figure 1A showing Control (Cont.) proliferative (Prolif.) and arrested (Arrest) cells. **(B)** Cell and nuclear size were calculated on sub-populations of cells that appeared to form clonal out growths. Quantification of cell size and nuclear size from A, with a minimum of 100 cells analysed per condition. Shown are the mean+/- SD. Statistical significance was determined by one-way ANOVA (****p<0.0001, n.s = not significant). **(C)** LeGo RGB colour guided clonal cell tracking system was used to track clonal dynamics after cisplatin pulse treatment. Cells were treated as per Figure 1A, with clonal identification and quantification **(D),** measured at 3 and 21-days post cisplatin exposure using Image J/Fiji (42-days post cisplatin exposure for NCI-H1573).

Figure 3 – In vivo validation of cisplatin effects on cell size and proliferation. (A) A549 and NCI-H1299 cells were injected subcutaneously with $2x10^6$ cells into the flanks of nude mice. Carboplatin (60 mg/kg) was delivered by a single tail-vein injection and tumours were harvest at 3 days post treatment and analysed by IHC for cell size and PCNA positive staining. Scale bar = 50µm **(B)** Quantitation of IHC images from A (control n=300, carbo n=400). Shown are the mean+/- SD. Statistical significance was determined by t-test (****p<0.0001, n.s = not significant).

Figure 4 – Comparative RNAseq analysis of FACS sorted cisplatin treated cells. (A) Schematic describing treatment, sorting and analysis pipeline. **(B)** Representative example of pre- and post-sorted control and cisplatin treated cells. **(C)** Hierarchical clustering of 3-independent biological repeat experiments of all altered genes identified by RNA-seq. **(D-F)** Volcano plots displaying significantly downregulated (blue) or upregulated (orange) genes and subsequent IPA canonical pathway analysis. Predictions of inhibition (blue) or activation (orange) or no change (white) states are based on the Ingenuity®Knowledge Base, which compares the expected change with experimental observation to all known upstream regulators. Variable stringent p-value (>1.3) and z-score (>0.5) cut-offs were used to limit pathways to top 7–8 most significant hits**. (G)** Hierarchical clustering of IPA comparative canonical analysis.

Figure 5 – Cell Cycle dependent regulation of cisplatin response. (A-B) Schematic of Palbociclib (Palbo) and Thymidine (Thy) protocols used synchronize FUCCI expressing A549 cells in G1, early and late S phase prior to 2h cisplatin pulse treatment. Specifically, G1 cells were released from Palbociclib and pulsed immediately with cisplatin (Palbo + Cis at 0h). Late G1 cells were pulsed with cisplatin at 6 h post release from released from Palbociclib (Palbo + Cis at 6h). Early S phase cells were treated with cisplatin 2 h prior to release from thymidine (Thy + Cis at -2h). Finally, mid-late S phase cells were pulsed with cisplatin at 4h post thymidine release (Thy + Cis at 4h). The fate of individual cells (n=50) The fate of individual cells (n=50) was tracked by time lapse microscopy, with images taken every 30 min for 72 h. **(C)** Quantification of cell fate outcomes from A; including G1 arrest before mitosis (G1 ABM), G1 arrest after mitosis (G1 AAM), death before mitosis (DBM) and death after mitosis (DAM) and Proliferative (Prolif.). **(D)** Quantitation of the total number of cell divisions overserved in each condition (n=50). Mean is shown, statistical significance was determined by one-way ANOVA (****p<0.0001, *p<0.05). **(E)** Schematic of optical window based longitudinal *in vivo* imaging of FUCCI A549 cells. **(F)** Representative 3D projection images from mice imaged at day 1 and day 7 with carboplatin (Carbo) or control (Saline). **(G)** Quantification of the proportion of red (G1), yellow (G1/S) and green (S/G2-M) cells found in tumours (n=3) from day 0 to 7.

Figure 6 – Dual DNA replication and damage biosensor analysis of cisplatin treated cells. (A) Representative maximum image projections of A549 cells co-expressing a mNeonGreen tagged PCNA chromobody (cyan) and a truncated version of 53BP1 tagged with mApple (trunc53BP1-mApple; red-hot LUT). Cells were imaged using confocal microscopy, with 10 µm thick z-stack (1 µm slice) taken every 30 min for 72 h. Scale bar 10 µm. (B) Quantification of the size and number of PCNA and 53BP1 foci for each cell shown in A. (C) 3D volume renders from cells in A for the indicated times, with cropped zoom areas (right image). White arrows indicate 53BP1 foci that reduce in size over time (min). Scale bars 5 µm and 1 µm for left and right panels respectively.

Figure 7 – Inhibition of PARP reduces ability of early S phase cells to maintain proliferative capacity. (A) Schematic of Palbociclib (Palbo) and Thymidine (Thy) protocols used synchronize FUCCI expressing A549 cells in G1, early and late S phase prior to Olaparib

(PARPi; 1 µM) and 2h cisplatin (5 µg/ml) pulse treatment. The fate of (n=50) individual cells was tracked by time-lapse microscopy, with images taken every 30 min for 72 h. Quantitation of the total number of cell divisions **(B)** and G1 length after **(C)** first mitotic division overserved in each condition. Statistical significance was determined by one-way ANOVA (***p<0.001, *p<0.05). **(D)** Quantification of cell fate outcomes from A; including G1 arrest before mitosis (G1 ABM), G1 arrest after mitosis (G1 AAM), death before mitosis (DBM) and death after mitosis (DAM) and Proliferative (Prolif.). **(E)** Fluorescent imaging of asynchronous A549 dual biosensor cells pulsed with cisplatin for 2 h. The percentage of cells with less than 5 (<5) or more than 15 (>15) (<5) 53BP1 foci/cell after cisplatin treatment are shown. A minimum of 250 cells per timepoint and condition were counted from (n=3) biological repeats. Statistical significance was determined by two-way ANOVA (*p<0.05). **(F)** Thymidine synchronized cells treated as per A, were harvested, and analysed for cell size and γ-H2AX by flow cytometry. Representative FACS plots and quantification from (n=3) biological repeats are shown. Statistical significance was determined by one-way ANOVA (***p<0.001, *p<0.05).

Figure 8 – Schematic outlining cell cycle dependence of cisplatin recovery. Briefly, cells exposed in G1 undergo S/G2 phase arrest, marked by high levels of P70S6K, p53 and p21, which results in a stable and permanent cell cycle exit from G2 phase. Cells in late S phase, likely receive platinum adducts in areas of already duplicated DNA, with error-prone non-homologous end joining (NHEJ) favoured over homologous recombination (HR). Combined with an increase in cells undergoing aberrant division, results in daughter cells displaying higher rates of damage during replication resulting in S/G2 arrest and senescence. In contrast, cells in late G1/ early S phase, have the opportunity to detect and repair damage by HR during the first cycle, thereby increasing chances daughter cells will successfully complete and repair damage, thereby allowing continued proliferation.

Supplementary Figures and Tables

Figure 2 Supplement 1: (A) Representative images and quantification of colony formation assays for A549, NCI-H1573 and NCI-H1299 cells treated with or without cisplatin. Colonies were fixed, stained and counted 10 (A549 and NCI-H1299) or 14 days (NCI-H1573) after

cisplatin exposure. Scale bar = 100µm. Shown are the mean +/- SD of 3 biological repeats. Statistical significance was determined by Students t-test (****p<0.0001,***p<0.001,**p<0.01). **(B)** Representative images and quantification of A549, NCI-H1573 and CI-H1299 cells 3 days after cisplatin exposure stained for beta-galactosidase. Scale bar = 100µm. Shown are the mean +/- SD of 3 biological repeats. **(C)** FACS analysis of P21, P16 and beta galactosidase activity levels (C_{12}FDG) versus "cell size" (FSC) at 3-days after cisplatin exposure. Shown are the mean +/- SD of 3 biological repeats.

Figure 4 Supplement 1: (A) Cytoscape Enrichment map of curated gene sets of canonical pathways for Proliferative versus Arrested cells. Each node represents a gene set and each line connecting nodes a gene "common" to both nodes. Shown are gene sets enriched in proliferative (Red) and Arrested (blue). The size of the node represents the NES score of that particular gene set. **(B)** GSEA Enrichment plots for Proliferative versus Arrest cells (curated gene sets for canonical pathways). From left to right and top to bottom: Cell Cycle, Homology Directed Repair, Fanconi Pathway and ATR Pathway. The green curve corresponds to the ES (enrichment score) curve, which is the running sum of the weighted enrichment score obtained from GSEA software, while the normalized enrichment score (NES) and the corresponding FDR (false discovery rate) value are reported within each graph.

Figure 5 Supplement 1: (A) Representative images of A549 FUCCI expressing cells treated with (Cisplatin) or without (Control) 5µg/ml cisplatin for 2 h and then followed by time lapse microscopy. Images were taken every 20 min for 3 days. Arrows indicate mother and daughter cells followed through time. **(B,C)** Single cell fate maps from cells (n=50) control and (n=100) cisplatin treated cells. **(D)** Quantification of cell cycle phase length from data generated in B and C. Statistical significance was determined by one-way ANOVA (****p<0.0001, n.s = not significant).

Figure 6 Supplement 1: (A) Quantification of the size and number of PCNA and 53BP1 foci for additional cells as per Figure 6A and 6B. (B) Number of 53BP1 foci in cells from early S and mid/late S phase (n=4), were temporally aligned base on entry into and exit from the first mitosis. (C) Representative images of the first mitosis observed in cells that were in mid

S-phase at the time of cisplatin exposure. White arrow heads indicate micronuclei (mn) in daughter cells, cf= cytokinesis failure. Scale bar = 10 µm.

References:

Anders, S., and Huber, W. (2010). Differential expression analysis for sequence count data. *Genome Biol* 11, R106. doi:10.1186/gb-2010-11-10-r106.

Andersson, A., Fagerberg, J., Lewensohn, R., and Ehrsson, H. (1996). Pharmacokinetics of Cisplatin and Its Monohydrated Complex in Humans. *J Pharm Sci* 85, 824–827. doi:10.1021/js960037a.

Barr, A. R., Cooper, S., Heldt, F. S., Butera, F., Stoy, H., Mansfeld, J., et al. (2017). DNA damage during S-phase mediates the proliferation-quiescence decision in the subsequent G1 via p21 expression. *Nat Commun* 8, ncomms14728. doi:10.1038/ncomms14728.

Baus, F., Gire, V., Fisher, D., Piette, J., and Dulić, V. (2003). Permanent cell cycle exit in G2 phase after DNA damage in normal human fibroblasts. *The EMBO Journal* 22, 3992 4002. doi:10.1093/emboj/cdg387.

Burgess, A., Lorca, T., and Castro, A. (2012). Quantitative live imaging of endogenous DNA replication in mammalian cells. *Plos One* 7, e45726. doi:10.1371/journal.pone.0045726.

Burgess, A., Rasouli, M., and Rogers, S. (2014). Stressing Mitosis to Death. *Frontiers Oncol* 4, 140. doi:10.3389/fonc.2014.00140.

Caldon, C. E., and Burgess, A. (2019). Label free, quantitative single-cell fate tracking of time-lapse movies. *Methodsx* 6, 2468–2475. doi:10.1016/j.mex.2019.10.014.

Chan, Y. W., Fugger, K., and West, S. C. (2017). Unresolved recombination intermediates lead to ultra-fine anaphase bridges, chromosome breaks and aberrations. *Nat Cell Biol* 20, 92–103. doi:10.1038/s41556-017-0011-1.

Chan, Y. W., and West, S. C. (2018). A new class of ultrafine anaphase bridges generated by homologous recombination. *Cell Cycle* 17, 1–9. doi:10.1080/15384101.2018.1515555.

Charrasse, S., Gharbi-Ayachi, A., Burgess, A., Vera, J., Hached, K., Raynaud, P., et al. (2017). Ensa controls S-phase length by modulating Treslin levels. *Nat Commun* 8, 206. doi:10.1038/s41467-017-00339-4.

Danecek, P., and McCarthy, S. A. (2017). BCFtools/csq: haplotype-aware variant consequences. *Bioinformatics* 33, btx100. doi:10.1093/bioinformatics/btx100.

865 Dobin, A., Davis, C. A., Schlesinger, F., Drenkow, J., Zaleski, C., Jha, S., et al. (2013). STAR:
866 ultrafast universal RNA-seq aligner. *Bioinformatics* 29, 15–21.
867 doi:10.1093/bioinformatics/bts635.

868 Enoiu, M., Jiricny, J., and Schärer, O. D. (2012). Repair of cisplatin-induced DNA interstrand
869 crosslinks by a replication-independent pathway involving transcription-coupled repair
870 and translesion synthesis. *Nucleic Acids Res* 40, 8953–64. doi:10.1093/nar/gks670.

871 Gligorijevic, B., Kedrin, D., Segall, J. E., Condeelis, J., and Rheenen, J. van (2009). Dendra2
872 Photoswitching through the Mammary Imaging Window. *J Vis Exp Jove*, 1278.
873 doi:10.3791/1278.

874 Gonzalez-Rajal, A., Hastings, J. F., Watkins, D. N., Croucher, D. R., and Burgess, A. (2020).
875 Breathing New Life into the Mechanisms of Platinum Resistance in Lung
876 Adenocarcinoma. *Frontiers Cell Dev Biology* 8, 305. doi:10.3389/fcell.2020.00305.

877 Hastings, J. F., Rajal, A. G., Latham, S. L., Han, J. Z., McCloy, R. A., O'Donnell, Y. E., et al.
878 (2020). Analysis of pulsed cisplatin signalling dynamics identifies effectors of resistance in
879 lung adenocarcinoma. *Elife* 9, e53367. doi:10.7554/elife.53367.

880 Hayashi, M. T., and Karlseder, J. (2013). DNA damage associated with mitosis and
881 cytokinesis failure. *Oncogene* 32, 4593–4601. doi:10.1038/onc.2012.615.

882 Herbst, R. S., Morgensztern, D., and Boshoff, C. (2018). The biology and management of
883 non-small cell lung cancer. *Nature* 553, 446–454. doi:10.1038/nature25183.

884 Hsu, C.-H., Altschuler, S. J., and Wu, L. F. (2019). Patterns of Early p21 Dynamics Determine
885 Proliferation-Senescence Cell Fate after Chemotherapy. *Cell* 178, 361-373.e12.
886 doi:10.1016/j.cell.2019.05.041.

887 Johnson, T. G., Schelch, K., Lai, K., Marzec, K. A., Kennerson, M., Grusch, M., et al. (2020).
888 YB-1 Knockdown Inhibits the Proliferation of Mesothelioma Cells through Multiple
889 Mechanisms. *Cancers* 12, 2285. doi:10.3390/cancers12082285.

890 Karanam, K., Kafri, R., Loewer, A., and Lahav, G. (2012). Quantitative live cell imaging reveals
891 a gradual shift between DNA repair mechanisms and a maximal use of HR in mid S phase.
892 *Mol Cell* 47, 320–9. doi:10.1016/j.molcel.2012.05.052.

893 Kedrin, D., Gligorijevic, B., Wyckoff, J., Verkhusha, V. V., Condeelis, J., Segall, J. E., et al.
894 (2008). Intravital imaging of metastatic behavior through a mammary imaging window.
895 *Nat Methods* 5, 1019–1021. doi:10.1038/nmeth.1269.

896 Kelland, L. (2007). The resurgence of platinum-based cancer chemotherapy. *Nat Rev Cancer*
897 7, 573–584. doi:10.1038/nrc2167.

898 Love, M. I., Huber, W., and Anders, S. (2014). Moderated estimation of fold change and
899 dispersion for RNA-seq data with DESeq2. *Genome Biol* 15, 550. doi:10.1186/s13059-014-
900 0550-8.

Mamdani, H., and Jalal, S. I. (2016). DNA repair in lung cancer: potential not yet reached. *Lung Cancer Management* 5, 5–8. doi:10.2217/lmt-2016-0004.

Marini, K. D., Croucher, D. R., McCloy, R. A., Vaghjiani, V., Gonzalez-Rajal, A., Hastings, J. F., et al. (2018). Inhibition of activin signaling in lung adenocarcinoma increases the therapeutic index of platinum chemotherapy. *Sci Transl Med* 10, eaat3504. doi:10.1126/scitranslmed.aat3504.

McCloy, R. A., Rogers, S., Caldon, C. E., Lorca, T., Castro, A., and Burgess, A. (2014). Partial inhibition of Cdk1 in G 2 phase overrides the SAC and decouples mitotic events. *Cell Cycle Georget Tex* 13, 1400–12. doi:10.4161/cc.28401.

Mootha, V. K., Lindgren, C. M., Eriksson, K.-F., Subramanian, A., Sihag, S., Lehar, J., et al. (2003). PGC-1α-responsive genes involved in oxidative phosphorylation are coordinately downregulated in human diabetes. *Nat Genet* 34, 267–273. doi:10.1038/ng1180.

Murai, J., and Pommier, Y. (2018). PARP Trapping Beyond Homologous Recombination and Platinum Sensitivity in Cancers. *Annu Rev Cancer Biology* 3, 1–20. doi:10.1146/annurev-cancerbio-030518-055914.

Nobis, M., Herrmann, D., Warren, S. C., Kadir, S., Leung, W., Killen, M., et al. (2017). A RhoA-FRET Biosensor Mouse for Intravital Imaging in Normal Tissue Homeostasis and Disease Contexts. *Cell Reports* 21, 274–288. doi:10.1016/j.celrep.2017.09.022.

Pertea, M., Pertea, G. M., Antonescu, C. M., Chang, T.-C., Mendell, J. T., and Salzberg, S. L. (2015). StringTie enables improved reconstruction of a transcriptome from RNA-seq reads. *Nat Biotechnol* 33, 290–295. doi:10.1038/nbt.3122.

Ritsma, L., Steller, E. J. A., Ellenbroek, S. I. J., Kranenburg, O., Rinkes, I. H. M. B., and Rheenen, J. van (2013). Surgical implantation of an abdominal imaging window for intravital microscopy. *Nat Protoc* 8, 583–594. doi:10.1038/nprot.2013.026.

Saldivar, J. C., Hamperl, S., Bocek, M. J., Chung, M., Bass, T. E., Cisneros-Soberanis, F., et al. (2018). An intrinsic S/G 2checkpoint enforced by ATR. *Science* 361, 806 810. doi:10.1126/science.aap9346.

Salvador-Barbero, B., Álvarez-Fernández, M., Zapatero-Solana, E., Bakkali, A. E., Menéndez, M. del C., López-Casas, P. P., et al. (2020). CDK4/6 Inhibitors Impair Recovery from Cytotoxic Chemotherapy in Pancreatic Adenocarcinoma. *Cancer Cell* 37, 340-353.e6. doi:10.1016/j.ccell.2020.01.007.

Sarlós, K., Biebricher, A., Petermann, E. J. G., Wuite, G. J. L., and Hickson, I. D. (2017). Knotty Problems during Mitosis: Mechanistic Insight into the Processing of Ultrafine DNA Bridges in Anaphase. *Cold Spring Harb Sym* 82, 187–195. doi:10.1101/sqb.2017.82.033647.

Schmidt, U., Weigert, M., Broaddus, C., and Myers, G. (2018). Cell Detection with Star-convex Polygons. *Arxiv*, 265–273. doi:10.1007/978-3-030-00934-2_30.

938 Shannon, P., Markiel, A., Ozier, O., Baliga, N. S., Wang, J. T., Ramage, D., et al. (2003).
939 Cytoscape: A Software Environment for Integrated Models of Biomolecular Interaction
940 Networks. *Genome Res* 13, 2498–2504. doi:10.1101/gr.1239303.

941 Sherry, S. T., Ward, M.-H., Kholodov, M., Baker, J., Phan, L., Smigielski, E. M., et al. (2001).
942 dbSNP: the NCBI database of genetic variation. *Nucleic Acids Res* 29, 308–311.
943 doi:10.1093/nar/29.1.308.

944 Slyskova, J., Sabatella, M., Ribeiro-Silva, C., Stok, C., Theil, A. F., Vermeulen, W., et al. (2018).
945 Base and nucleotide excision repair facilitate resolution of platinum drugs-induced
946 transcription blockage. *Nucleic Acids Res* 46, 9537–9549. doi:10.1093/nar/gky764.

947 Smogorzewska, A. (2019). Fanconi Anemia: A Paradigm for Understanding DNA Repair
948 During Replication. *Blood* 134, SCI-32-SCI-32. doi:10.1182/blood-2019-121229.

949 Spies, J., Lukas, C., Somyajit, K., Rask, M.-B., Lukas, J., and Neelsen, K. J. (2019). 53BP1
950 nuclear bodies enforce replication timing at under-replicated DNA to limit heritable DNA
951 damage. *Nat Cell Biol* 21, 1–11. doi:10.1038/s41556-019-0293-6.

952 Stewart, D. J. (2007). Mechanisms of resistance to cisplatin and carboplatin. *Crit Rev Oncol*
953 *Hemat* 63, 12–31. doi:10.1016/j.critrevonc.2007.02.001.

954 Subramanian, A., Tamayo, P., Mootha, V. K., Mukherjee, S., Ebert, B. L., Gillette, M. A., et al.
955 (2005). Gene set enrichment analysis: A knowledge-based approach for interpreting
956 genome-wide expression profiles. *P Natl Acad Sci Usa* 102, 15545–15550.
957 doi:10.1073/pnas.0506580102.

958 Swiecicki, P. L., Durm, G., Bellile, E., Bhangale, A., Brenner, J. C., and Worden, F. P. (2020). A
959 multi-center phase II trial evaluating the efficacy of palbociclib in combination with
960 carboplatin for the treatment of unresectable recurrent or metastatic head and neck
961 squamous cell carcinoma. *Invest New Drug* 38, 1550–1558. doi:10.1007/s10637-020-
962 00898-2.

963 Tutt, A., Tovey, H., Cheang, M. C. U., Kernaghan, S., Kilburn, L., Gazinska, P., et al. (2018).
964 Carboplatin in BRCA1/2-mutated and triple-negative breast cancer BRCAness subgroups:
965 the TNT Trial. *Nat Med* 24, 628–637. doi:10.1038/s41591-018-0009-7.

966 Urien, S., and Lokiec, F. (2004). Population pharmacokinetics of total and unbound plasma
967 cisplatin in adult patients. *British Journal of Clinical Pharmacology* 57, 756 763.
968 doi:10.1111/j.1365-2125.2004.02082.x.

969 Watt, L. P., Natsum, T., Saito, Y., Garzón, J., Dong, Q., Boteva, L., et al. (2020). The RIF1-Long
970 splice variant promotes G1 phase 53BP1 nuclear bodies to protect against replication
971 stress. *eLife*. doi:10.7554/elife.58020.

972 Weber, K., Bartsch, U., Stocking, C., and Fehse, B. (2008). A Multicolor Panel of Novel
973 Lentiviral “Gene Ontology” (LeGO) Vectors for Functional Gene Analysis. *Mol Ther* 16,
974 698–706. doi:10.1038/mt.2008.6.

975 Weber, K., Thomaschewski, M., Benten, D., and Fehse, B. (2012). RGB marking with lentiviral
976 vectors for multicolor clonal cell tracking. *Nat Protoc* 7, 839–849.
977 doi:10.1038/nprot.2012.026.

978 Weber, K., Thomaschewski, M., Warlich, M., Volz, T., Cornils, K., Niebuhr, B., et al. (2011).
979 RGB marking facilitates multicolor clonal cell tracking. *Nat Med* 17, 504–509.
980 doi:10.1038/nm.2338.

981 Yang, K. S., Kohler, R. H., Landon, M., Giedt, R., and Weissleder, R. (2015). Single cell
982 resolution in vivo imaging of DNA damage following PARP inhibition. *Sci Rep-uk* 5, 10129.
983 doi:10.1038/srep10129.

984

Figure 1

Rajal et al 2020

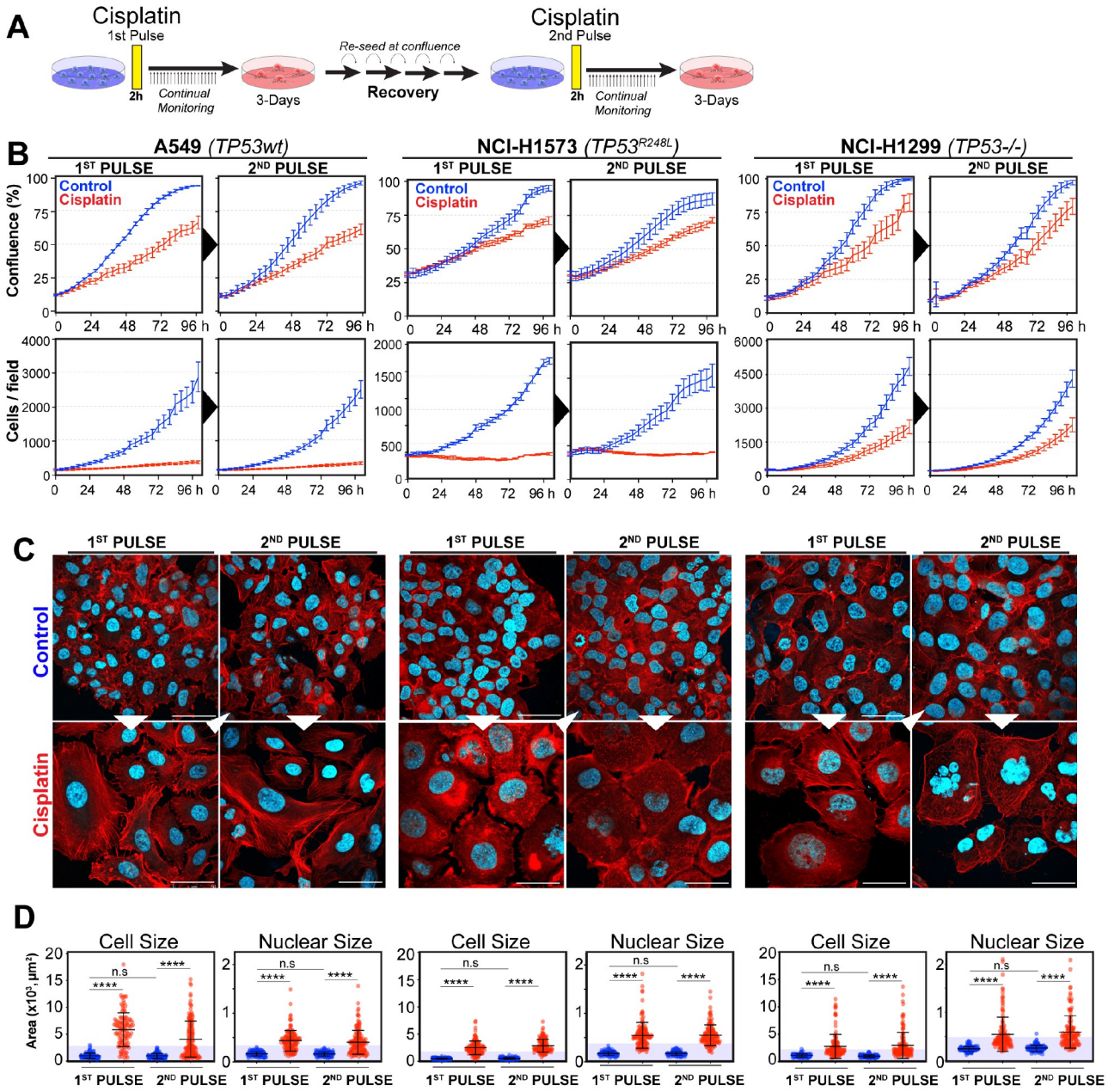

Figure 2

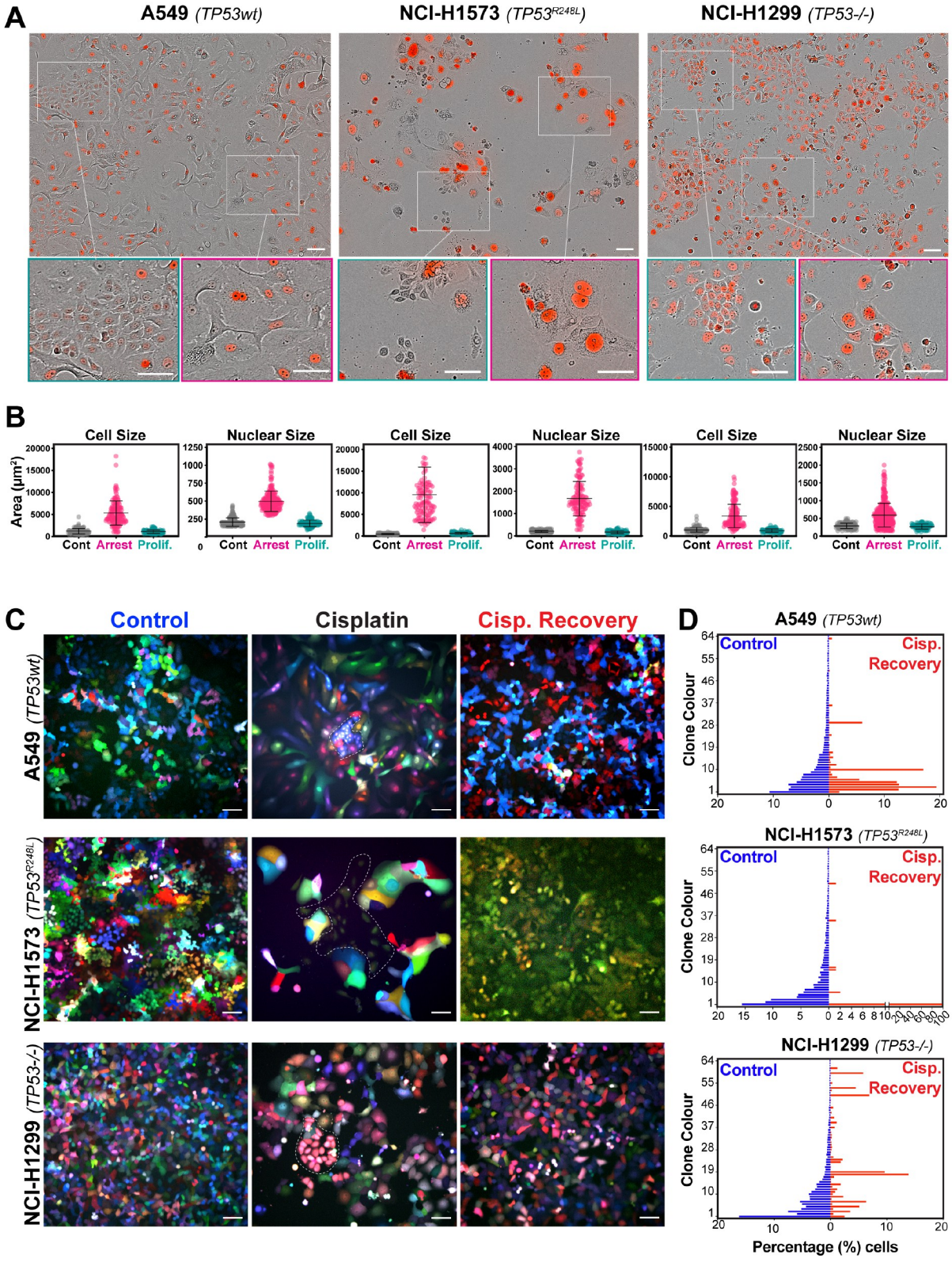

Figure 2 -Supplement 1

Rajal et al 2020

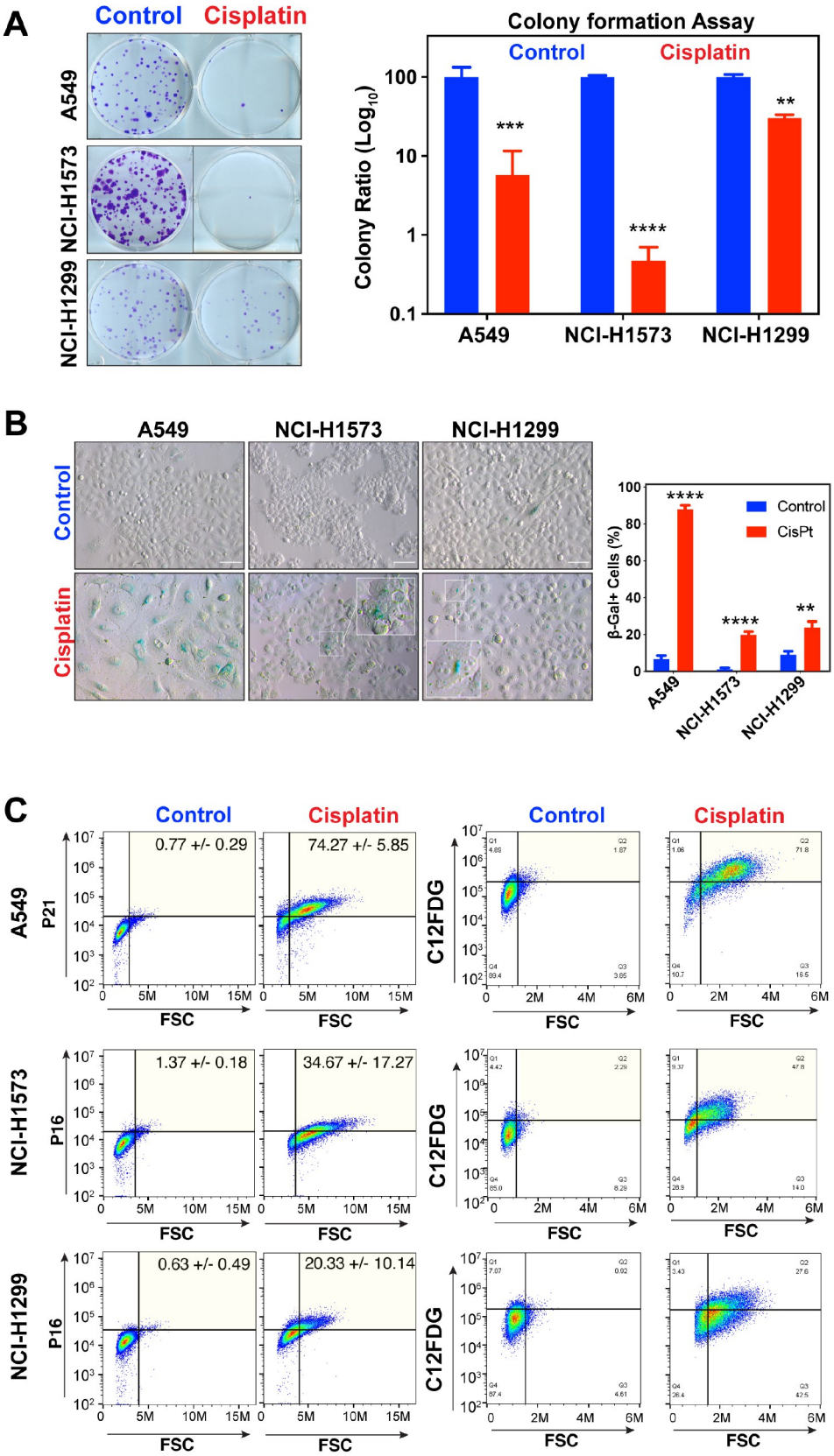

Figure 3

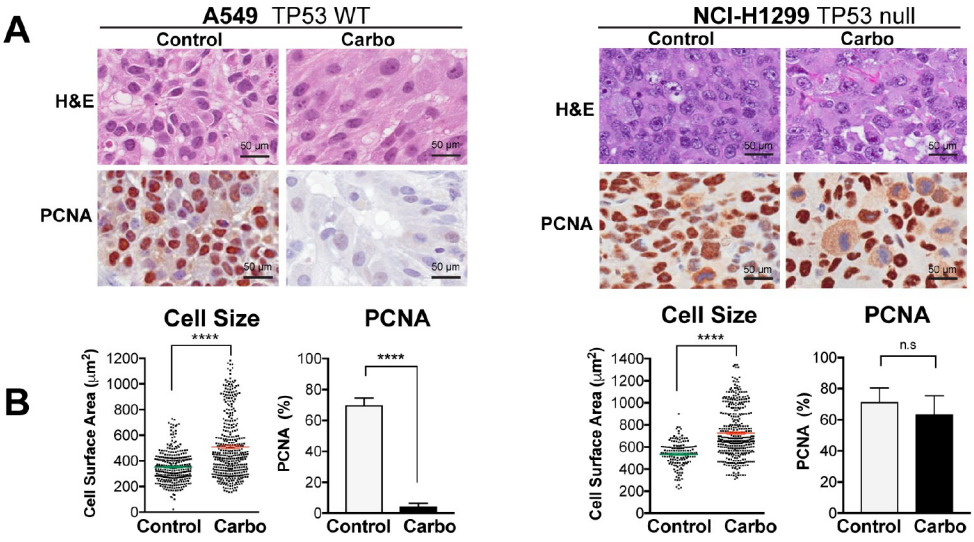

Figure 4

Rajal et al 2020

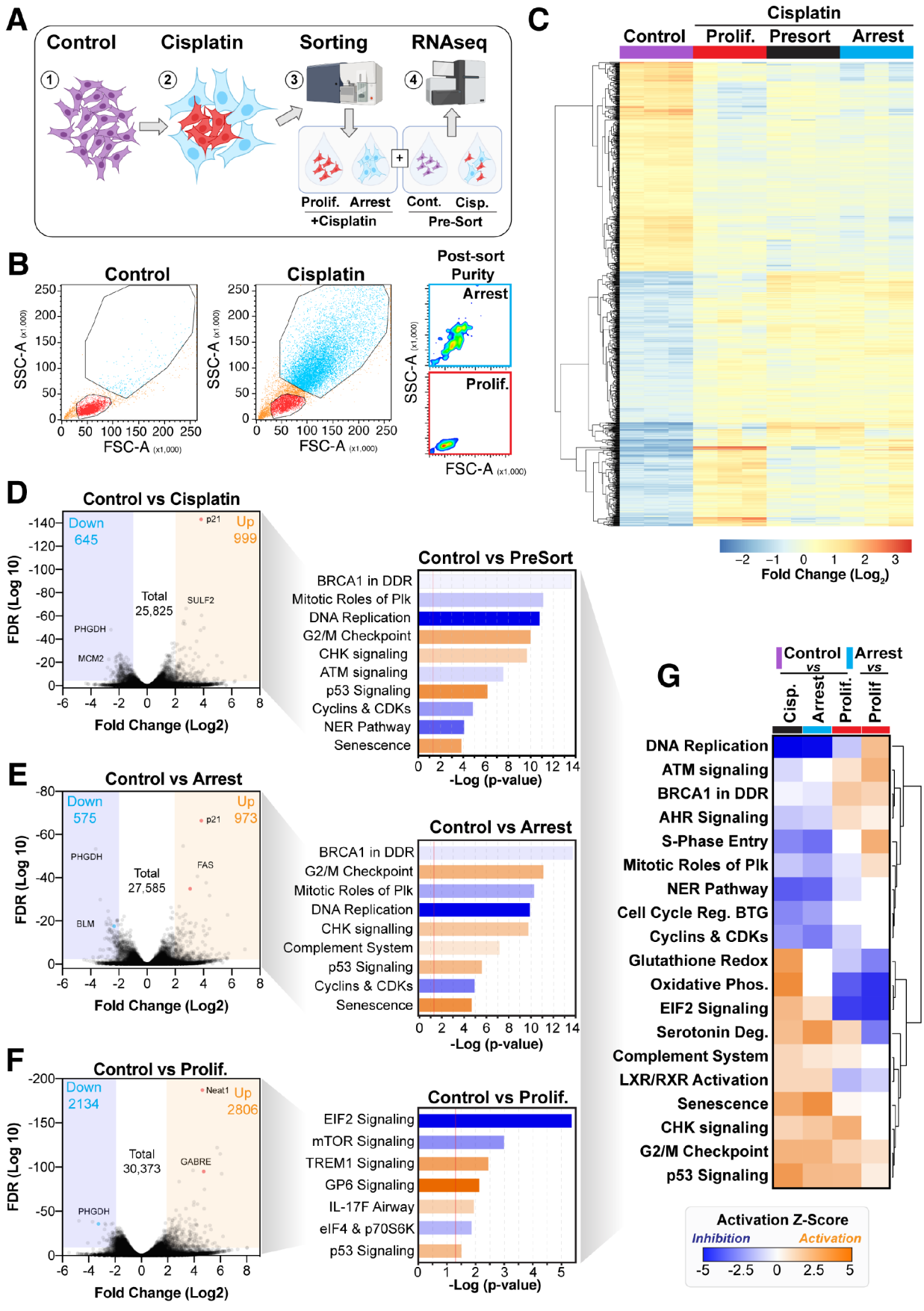

Figure 4 -Supplement 1

Rajal et al 2020

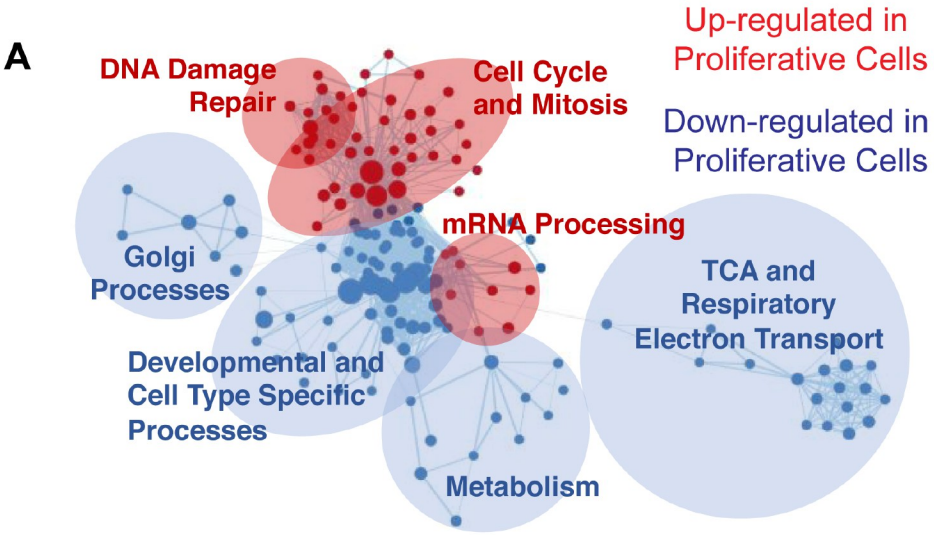

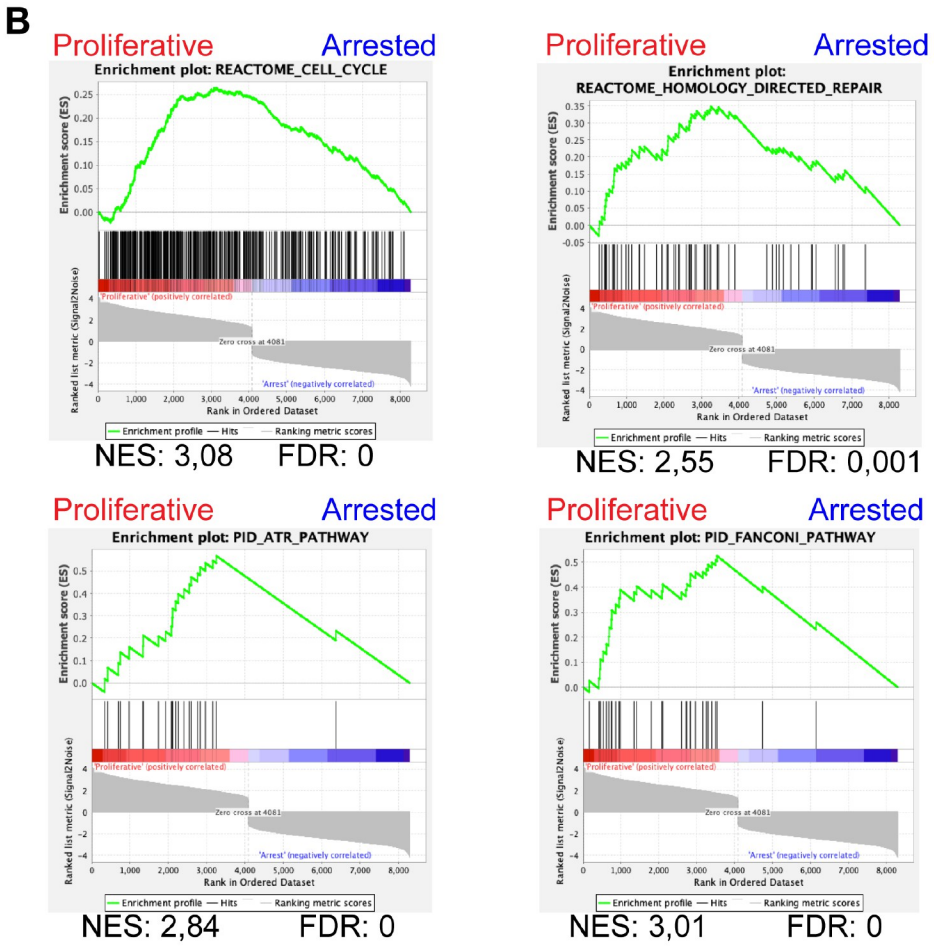

Figure 5

Rajal et al 2020

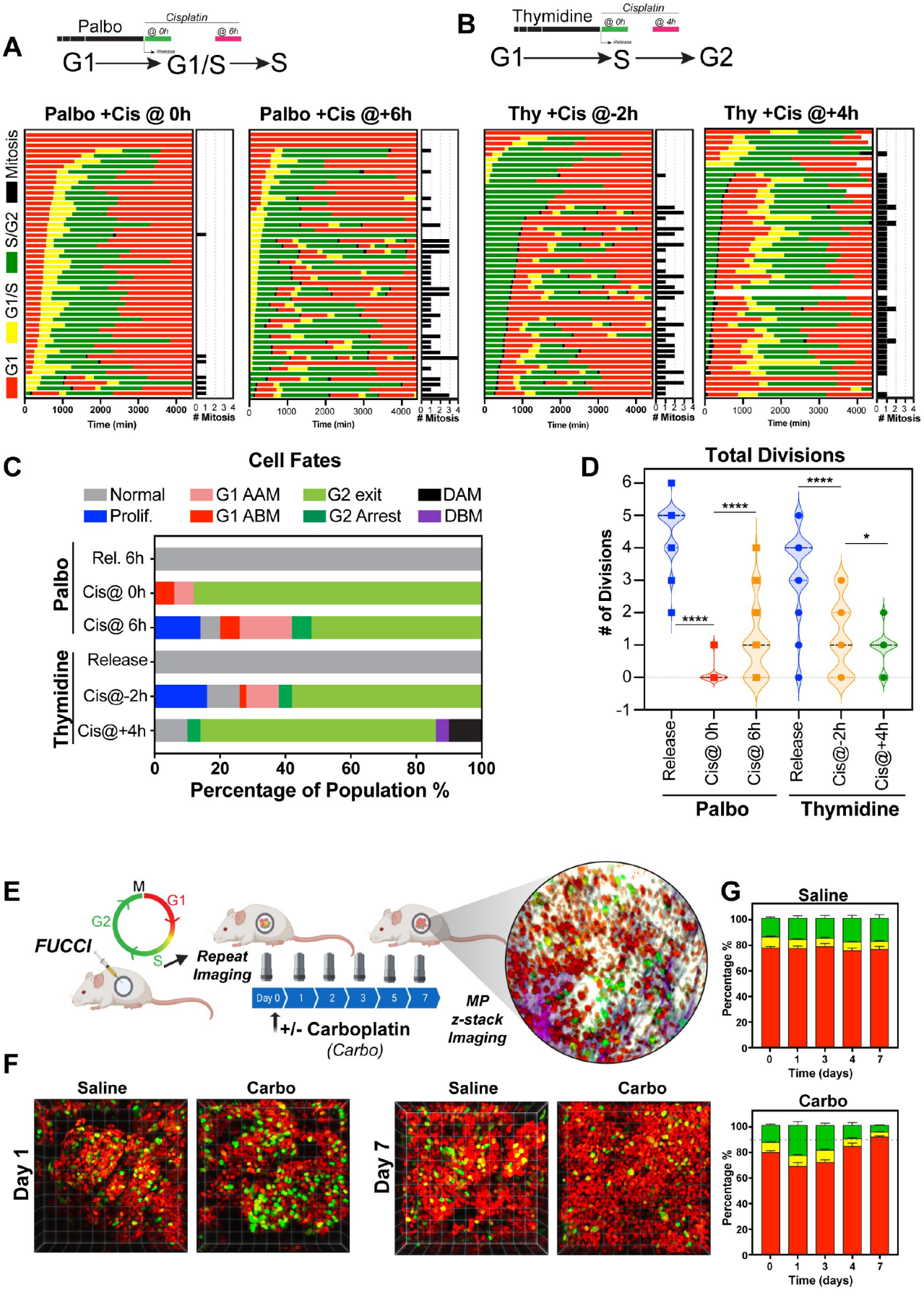

Figure 5 - Supplement 1

Rajal et al 2020

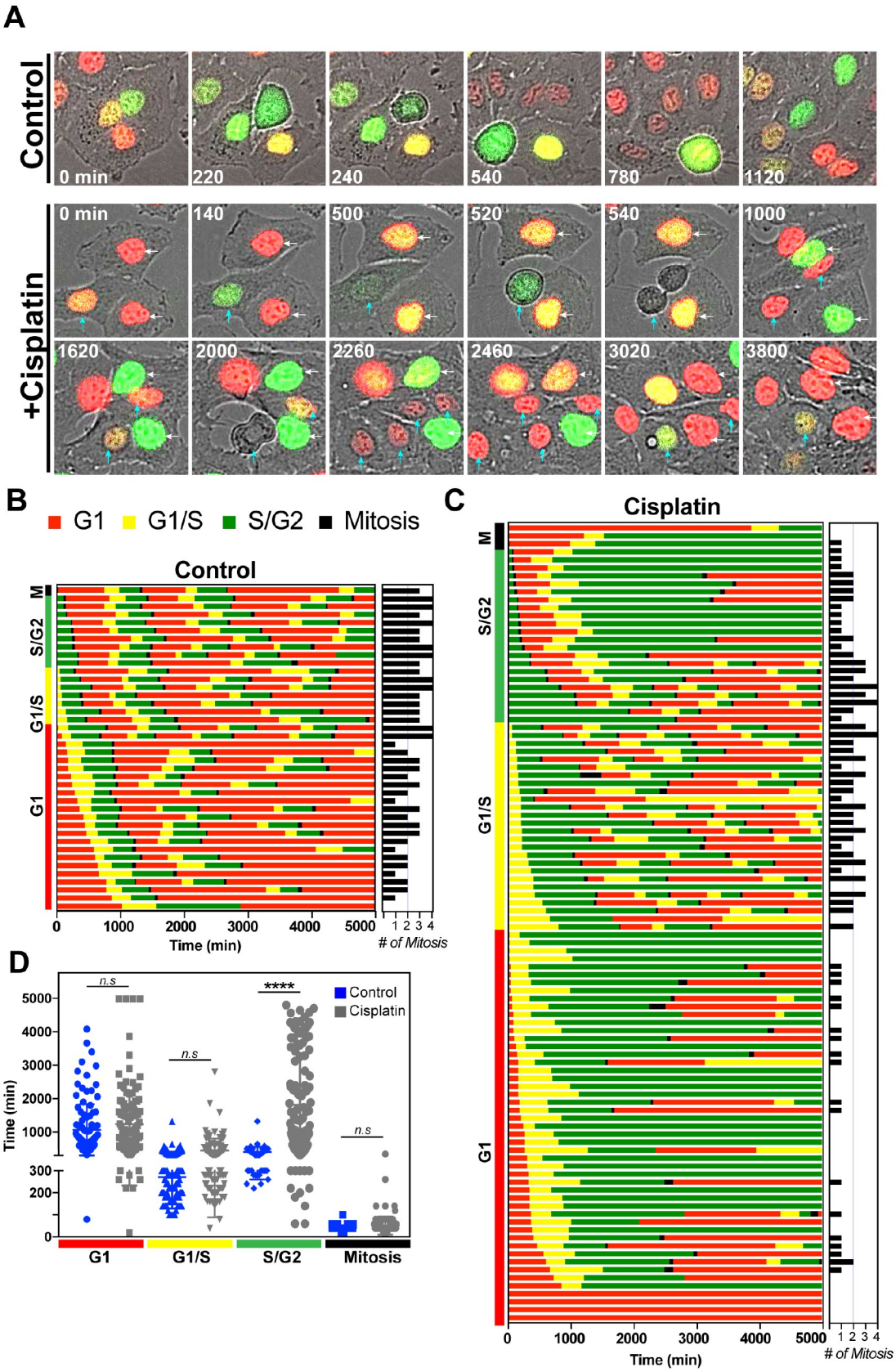

Figure 6

Rajal et al 2020

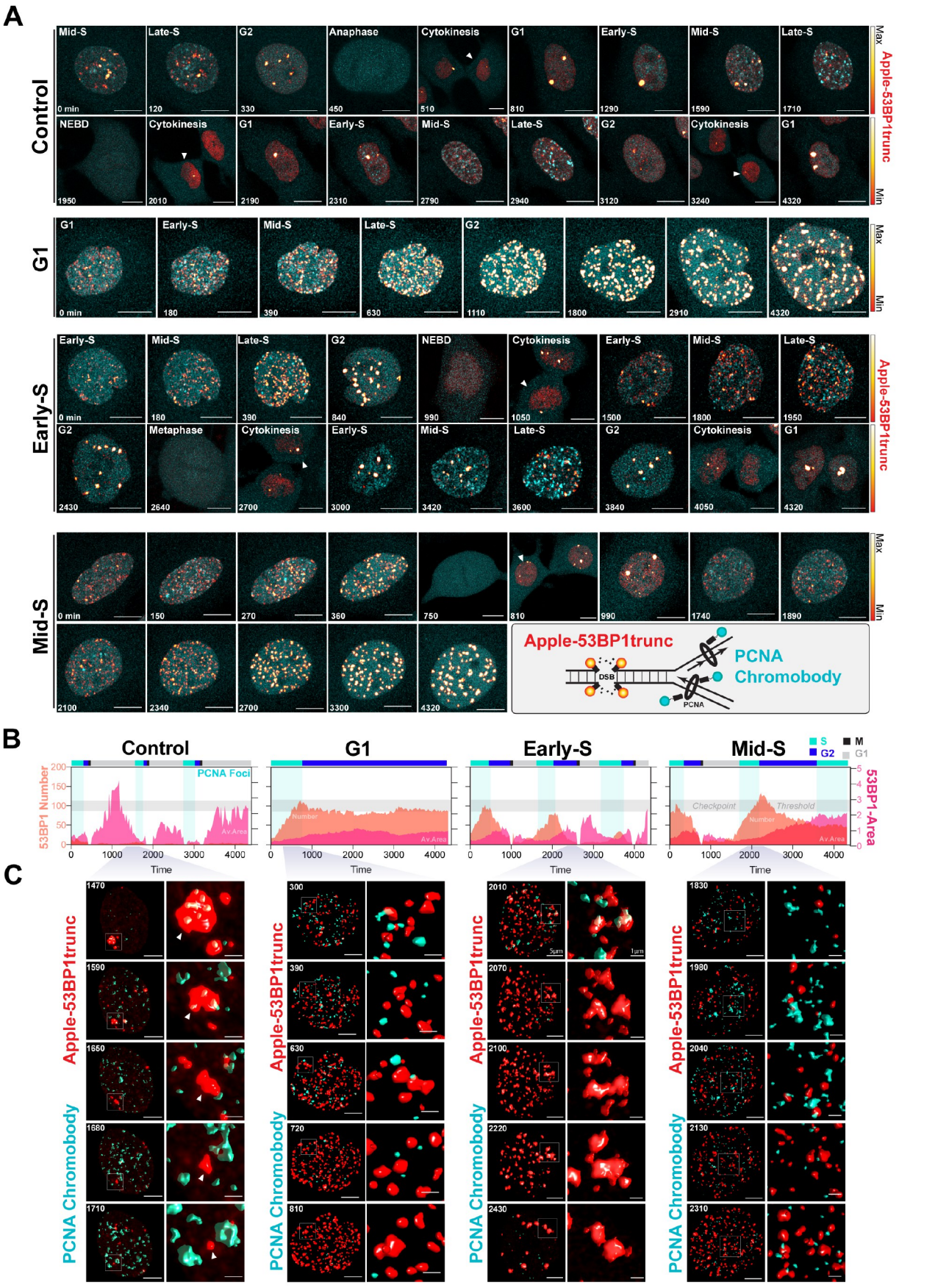

Figure 6 -Supplement 1

Rajal et al 2020

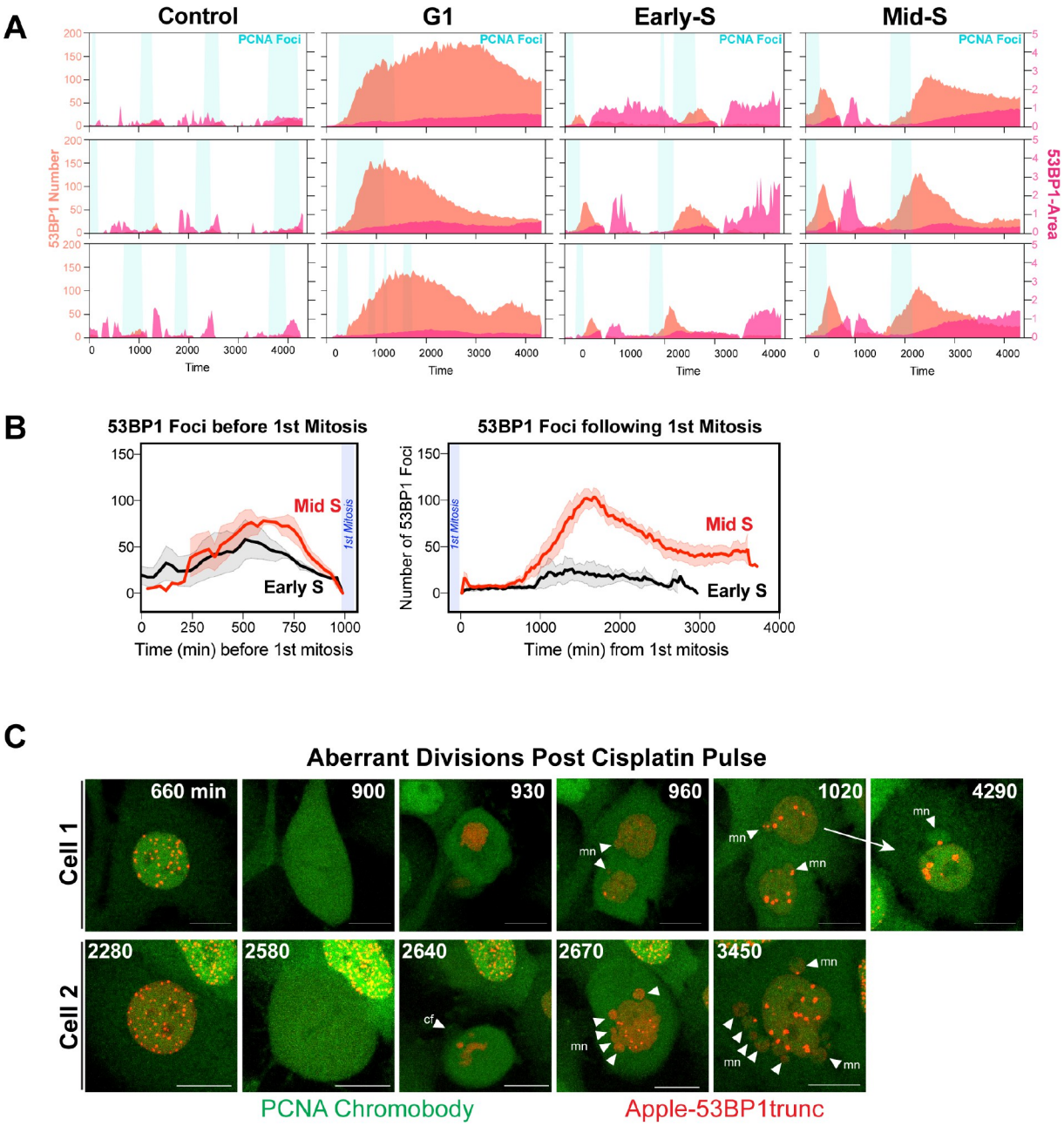

Figure 7

Rajal et al 2020

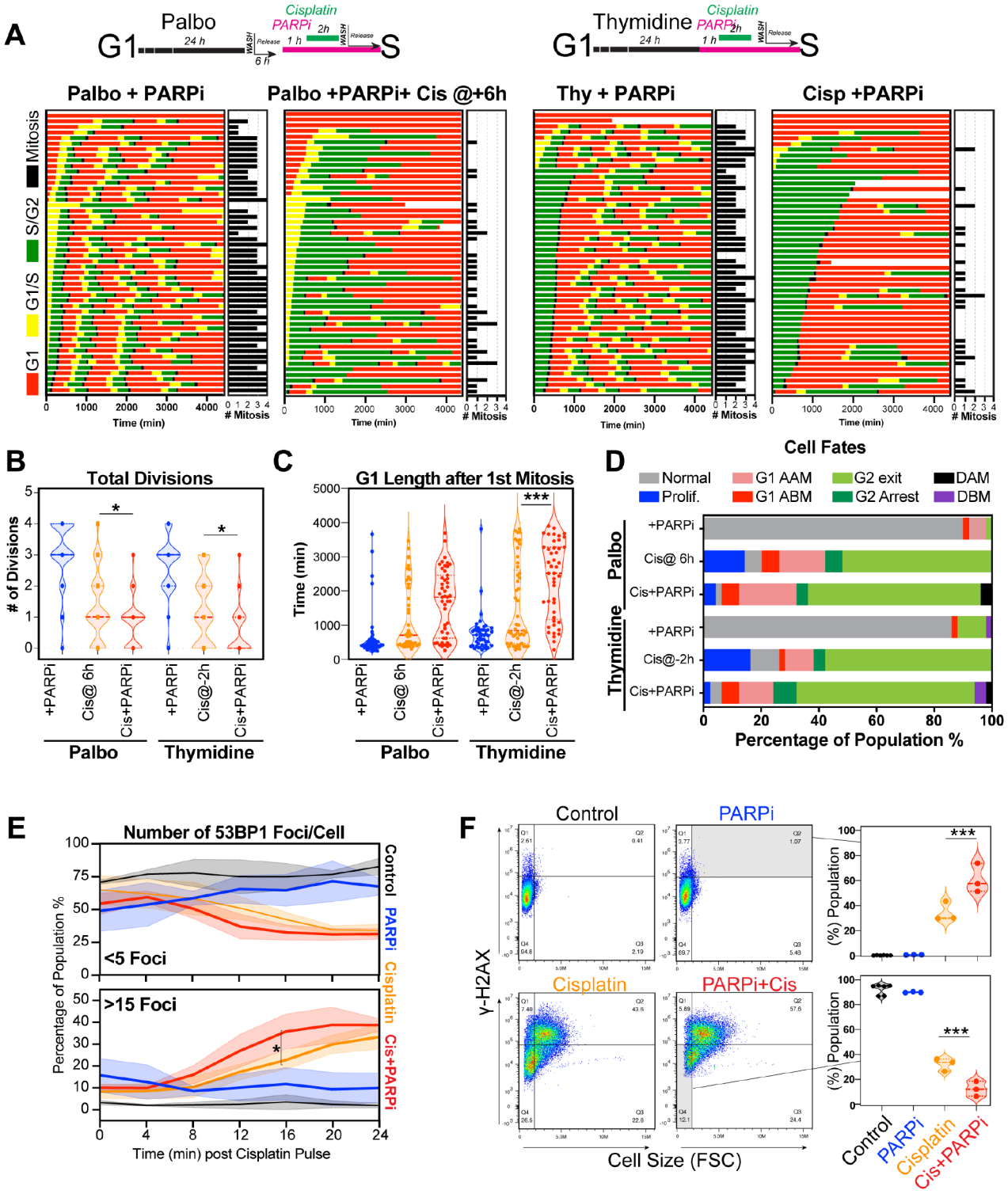

Figure 8

Rajal et al 2020